

Efficient black hole seed formation in low metallicity and dense stellar clusters with implications for JWST sources

M.C. Vergara^{1*}, A. Askar^{2**}, F. Flammini Dotti^{3,4,1}, D.R.G. Schleicher^{5,6}, A. Escala⁷, R. Spurzem^{1,8,9},
M. Giersz², J. Hurley^{10,11}, M. Arca Sedda^{12,13,14,15}, and N. Neumayer¹⁶

- ¹ Astronomisches Rechen-Institut, Zentrum für Astronomie, University of Heidelberg, Mönchhofstrasse 12-14, 69120, Heidelberg, Germany
- ² Nicolaus Copernicus Astronomical Center, Polish Academy of Sciences, Bartycka 18, 00-716 Warsaw, Poland
- ³ Department of Physics, New York University Abu Dhabi, PO Box 129188 Abu Dhabi, UAE
- ⁴ Center for Astrophysics and Space Science (CASS), New York University Abu Dhabi, PO Box 129188, Abu Dhabi, UAE
- ⁵ Dipartimento di Fisica, Sapienza Università di Roma, Piazzale Aldo Moro 5, 00185 Rome, Italy
- ⁶ Departamento de Astronomía, Facultad Ciencias Físicas y Matemáticas, Universidad de Concepción, Av. Esteban Iturra s/n Barrio Universitario, Casilla 160-C, Concepción, Chile
- ⁷ Departamento de Astronomía, Universidad de Chile, Casilla 36-D, Santiago, Chile
- ⁸ National Astronomical Observatories and Key Laboratory of Computational Astrophysics, Chinese Academy of Sciences, 20A Datun Rd., Chaoyang District, Beijing 100012, China
- ⁹ Kavli Institute for Astronomy and Astrophysics, Peking University, Yiheyuan Lu 5, Haidian Qu, 100871, Beijing, China
- ¹⁰ OzGrav: The ARC Centre of Excellence for Gravitational Wave Discovery, Hawthorn, VIC 3122, Australia
- ¹¹ Centre for Astrophysics and Supercomputing, Department of Physics and Astronomy, John Street, Hawthorn, Victoria, Australia 3122
- ¹² Gran Sasso Science Institute, Viale F. Crispi 7, I-67100 L'Aquila, Italy
- ¹³ Physics and Astronomy Department Galileo Galilei, University of Padova, Vicolo dell'Osservatorio 3, I-35122, Padova, Italy
- ¹⁴ INFN – Laboratori Nazionali del Gran Sasso, 67100 L'Aquila, (AQ), Italy
- ¹⁵ INAF – Osservatorio Astronomico d'Abruzzo, Via M. Maggini snc, 64100 Teramo, Italy
- ¹⁶ Max-Planck-Institut für Astronomie, Königstuhl 17, 69117 Heidelberg, Germany

Received September 15, XXXX; accepted March 16, YYYY

ABSTRACT

Context. Recent observations with the James Webb Space Telescope (JWST) have revealed the presence of young massive clusters (YMCs) as building blocks of the first galaxies during the first billion years of the Universe. They are not only important constituents of the galaxies, but also potential birth places of very massive stars (VMSs) and black hole (BH) seeds.

Aims. In this paper, we explore the stellar dynamics in extremely dense clusters with an initial half-mass density of $\rho_h \gtrsim 10^8 \text{ M}_\odot \text{ pc}^{-3}$ at very low metallicity. These densities are roughly comparable to some of the densest clusters found by JWST. Our detailed N -body and Monte Carlo simulations, which include stellar evolution, show that the formation of VMSs through collisions is unavoidable, with the resulting final masses reaching $\sim 5 \times 10^3$ to $4 \times 10^4 \text{ M}_\odot$. These simulations serve to verify the hypothesis that there is a critical mass scale at which collisions in the system become very efficient and thus VMSs and potentially intermediate-mass BHs (IMBHs) can form.

Methods. We use `NBODY6++GPU` and `MOCCA`, including the latest updates of the stellar evolution routines `SSE/BSE`, along with specific routines to handle the formation and dynamical evolution of VMSs.

Results. We show that dense star clusters rapidly form VMSs due to constant stellar bombardment. The VMSs eventually collapse and form a BH seed with masses ranging from a few 10^3 to a few 10^4 M_\odot in less than 4 Myr.

Conclusions. We discover a critical mass-density threshold in star clusters, beyond which the latter experience several runaway collisions, leading to the formation of massive BH seeds. Considering the ratio of stellar mass to critical mass for typical YMCs detected via JWST, we expect efficiencies in the range up to 10% for the so far detected clusters, thus corresponding to expected BH masses up to 10^5 M_\odot in case of their formation via collisions, we predict a relation for the BH mass that follows the shape of $\log(M_{\text{BH}} / \text{M}_\odot) = -0.76 + 0.76 \log(M / \text{M}_\odot)$. As a side product, the frequent formation of VMS may naturally explain the high amount of nitrogen found in galaxies at high redshift.

Key words. Methods: numerical, Galaxies: nuclei, Galaxies/quasars: supermassive black holes, Galaxies: star clusters: general

1. Introduction

Recently, the *James Webb Space Telescope* (JWST), has observed enigmatic "little red dots" (LRDs) (Kokorev et al. 2024; Akins et al. 2025), which are interpreted as either SMBHs heav-

ily obscured by dust or intensely star-forming dusty galaxies (Matthee et al. 2024; Napolitano et al. 2024). If these objects host active galactic nuclei (AGNs), it would indicate that most high-redshift galaxies indeed harbour central SMBHs (Greene et al. 2024). On the other hand, if dominated by star formation, LRDs could represent the most compact stellar systems ever observed (Guia et al. 2024).

* E-mail: Marcelo.C.Vergara@uni-heidelberg.de (MV)

** E-mail: askar@camk.edu.pl (AA)

As mentioned above, the currently enigmatic LRDs could well represent the most high redshift galaxies harboring a central SMBH (Greene et al. 2024), and/or the most compact stellar systems ever observed with central densities around $10^8 \text{ M}_\odot/\text{pc}^3$ (Guia et al. 2024). Some models also propose tidal disruption events (TDEs) of surrounding stars falling into an SMBH as potential explanations of their emission (Bellovary 2025). The estimated stellar to BH mass ratios of these objects are approximately two to three orders of magnitude higher than those observed in the local Universe, which has led to their classification as "overmassive" SMBHs (Goulding et al. 2023; Scoggins et al. 2023; Übler et al. 2024; Furtak et al. 2024; Juodžbalis et al. 2024). These overmassive SMBHs challenge existing models of BH growth, as they imply that BH grew extremely fast in the early Universe.

LRDs are not the only mysterious objects observed by JWST; the presence of young massive clusters (YMCs) in the early Universe also challenges current models of cosmic evolution. These stellar systems are extremely massive and dense, and their presence at high redshift implies that they must have formed within the first few hundred million years after the Big Bang (Vanzella et al. 2022a,b,c, 2023; Adamo et al. 2024; Mowla et al. 2024). Gas-rich dwarf galaxy mergers at high redshift have been suggested as a possible channel to form these massive and compact stellar systems (Renaud et al. 2015; Lahén et al. 2020b,a; Lahén et al. 2025). These highly dense stellar environments are ideal places for runaways collision to occur and form a VMS (Spitzer & Saslaw 1966; Spitzer & Stone 1967; Sanders 1970; Lee 1987; Quinlan & Shapiro 1990; Gürkan et al. 2004; Freitag et al. 2006a,b; Giersz et al. 2015; Vergara et al. 2023, 2024, 2025; Rantala & Naab 2025; Rantala et al. 2025) and also are suitable places for chemical self-enrichment (Vink 2018). These primordial dense stellar systems and their capability to form VMSs can be a possible explanation for other mysteries observations by the JWST, such as the high nitrogen-to-oxygen ratio in galaxies at high redshift (Charbonnel et al. 2023), which is around four times larger than in the solar vicinity (Cameron et al. 2023). Some examples of these galaxies with high nitrogen abundances are GN-z11 at redshift 10.6 (Bouwens et al. 2010; Tacchella et al. 2023; Nagele & Umeda 2023; Maiolino et al. 2024), CEERS-1019 at $z = 8.679$ (Larson et al. 2023; Marques-Chaves et al. 2024) and the most distant one to the date MOM-z14 at $z = 14.44$ (Naidu et al. 2025).

To explain the formation of VMSs and SMBHs, several scenarios had been proposed in the literature (Rees 1978, 1984). One prominent scenario involves the remnants of Population III (Pop III) stars, which form in metal-free clouds and accrete mass onto their cores (Bond et al. 1984; Omukai & Nishi 1998; Madau & Rees 2001; Volonteri et al. 2003; Tan & McKee 2004; Ricarte & Natarajan 2018; Mestichelli et al. 2024; Reinoso et al. 2025; Solar et al. 2025). Pop III stars under rapid rotation are potential source of nitrogen enrichment (Tsiatsiou et al. 2024; Nandal et al. 2024). Alternatively, the direct collapse of gas clouds (Loeb & Rasio 1994; Begelman et al. 2006; Lodato & Natarajan 2006; Chon & Omukai 2024), possibly through a quasi-star phase (Begelman 2010), has been suggested as another viable pathway. Stellar dynamics have been proposed as a possible pathway (Portegies Zwart et al. 1999a; Portegies Zwart & McMillan 2002; Reinoso et al. 2018a, 2020; Alister Seguel et al. 2020; Vergara et al. 2021, 2023, 2024, 2025).

The early attempts to explain the high luminosities observed in galactic centers relied on analytical models. Spitzer & Saslaw (1966); Spitzer & Stone (1967) demonstrated that luminosities of $\sim 10^{43} \text{ erg s}^{-1}$ can arise in dense star clusters of 10^8 M_\odot

within a radius of $\sim 0.1 \text{ pc}$. Similarly, Sanders (1970) showed that VMS could form in stellar systems with short relaxation times. VMS formation via collisions was first predicted using Fokker-Planck models, which indicated that a massive star naturally forms at the cluster core due to the deep gravitational potential (Lee 1987). Later, Quinlan & Shapiro (1990) proposed that dense galactic nuclei could host stars with masses of thousands of solar masses, potentially seeding SMBHs. Monte Carlo simulations by Gürkan et al. (2004) revealed that dense clusters undergo core collapse faster than the lifetime of a massive star, enabling sustained mass growth before collapse. In particular, clusters with over a million stars exhibit high collision rates, facilitating the formation of $\sim 10^3 \text{ M}_\odot$ stars that may collapse into IMBHs (Freitag et al. 2006b,a; Giersz et al. 2015). Direct N -body simulations have also produced massive stars of hundreds of solar masses (Portegies Zwart et al. 1999a, 2004). The first million-particle N -body simulation, DRAGON (Wang et al. 2016), marked a significant milestone. Subsequent studies, including the DRAGON-II simulations by Arca Sedda et al. (2023, 2024a,b), have investigated the formation of IMBHs in star clusters with central densities of approximately $10^5 \text{ M}_\odot \text{ pc}^{-3}$. Escala (2021) further argued that stellar systems become prone to global instability, thus conducive to massive object formation, if their average collision timescale is comparable to or shorter than their age, and discussed that primordial stellar clusters are ideal candidates to suffer such physical process. Vergara et al. (2023) has demonstrated with equal-mass star models that above a certain critical mass, defined when the average collision timescale is equal to their age, collapse becomes inevitable and massive objects can form in clusters with central densities up to $10^{10} \text{ M}_\odot \text{ pc}^{-3}$. This finding was expanded to different stellar systems, including not only NSCs, but also Globular Clusters (GCs) and Ultra-Compact Dwarf Galaxies (UCDs), covering different initial conditions, stellar initial mass functions, and evolutionary paths (Vergara et al. 2024). Using the critical mass framework, Liempi et al. (2025) reproduced the observed mass distribution of NSCs and SMBHs with semi-analytical models. Recently, Vergara et al. (2025) conducted one of the most computationally intensive million-particle simulations to date, with a central density of $> 10^7 \text{ M}_\odot \text{ pc}^{-3}$, forming an IMBH of $> 5 \times 10^4 \text{ M}_\odot$ within 5 Myr. Another scenario involves relativistic clusters, where stellar BH dynamics may facilitate SMBH formation (Shapiro & Teukolsky 1985; Lupi et al. 2014; Kroupa et al. 2020; Gaete et al. 2024; Bamber et al. 2025).

This paper is structured as follows: Section 2 presents the methodology and introduces the initial conditions. Section 3 presents the results. Finally, section 4 provides a summary of the conclusions along with a discussion of theoretical aspects.

2. Methodology

For this study, we performed simulations with the direct N -body code `NBODY6++GPU` and `MOCCA`¹, both codes have been widely compared (Giersz et al. 2008, 2015; Heggie 2014; Wang et al. 2016; Madrid et al. 2017; Kamlah et al. 2022a; Vergara et al. 2025), showing excellent agreement in stellar dynamics and individual stellar properties. Both share stellar and binary evolution recipes based on the SSE/BSE population synthesis codes Hurley et al. (2000, 2002, 2005) and updates to them by Banerjee et al. (2020); Kamlah et al. (2022a); Spurzem & Kamlah (2023) and Vergara et al. (2025).

¹ Monte Carlo Cluster simulAtor

2.1. Nbody6++GPU

NBODY6++GPU is a high-precision direct N -body code (Spurzem 1999; Wang et al. 2015; Spurzem & Kamlah 2023). It includes several algorithms to solve the stellar dynamics such as the Kustaanheimo-Stiefel regularization, an algorithm to solve close encounters and to form binaries (Stiefel & Kustaanheimo 1965), the chain regularization (Mikkola & Aarseth 1990, 1993), the 4th order Hermite integrator scheme with hierarchical block time-steps (McMillan 1986; Hut et al. 1995; Makino & Aarseth 1992; Makino 1999), the Ahmad-Cohen neighbour scheme which spatially splits the stellar hierarchy to speed up computational calculations (Ahmad & Cohen 1973), and parallelization and acceleration that allow large number of particles, using GPU (Wang et al. 2015), e.g. Wang et al. (2016); Arca Sedda et al. (2023, 2024a,b); Vergara et al. (2025). It enables realistic simulations of star clusters. The algorithms behind the treatment of the stellar dynamics are explained in more detail in the review article by Spurzem & Kamlah (2023) on collisional stellar systems.

2.2. MOCCA

MOCCA is a code for simulating the evolution of realistic star clusters (Giersz et al. 2013; Hypki & Giersz 2013). It is based on the Monte Carlo method developed by Hénon (1971), which was subsequently improved by Stodołkiewicz (1982, 1986) and Giersz (2001). This method combines the particle-based approach of direct N -body simulations with a statistical treatment of two-body relaxation, allowing for efficient computation of the long-term dynamical evolution of spherically symmetric star clusters. MOCCA includes treatments for important physical processes that drive cluster evolution, including stellar and binary evolution (SSE/BSE as in N -body), the effects of a galactic tidal field, and the direct integration of strong dynamical encounters using the FEWBODY code (Fregeau et al. 2004) for scattering experiments.

2.3. Initial conditions

We modeled 5 isolated clusters using a King density profile (King et al. 1968), with $W_0 = 6$, including a Kroupa initial mass function (IMF) (Kroupa 2001) with range $M_* = 0.08 - 150 M_\odot$. We varied the number of stars as $N = 5 \times 10^4, 10^5, 2 \times 10^5, 5 \times 10^5, 7.5 \times 10^5$, we do not include primordial binaries, the cluster half-mass radius varied as $R_h = 0.005, 0.01, 0.05$ pc and the absolute metallicity is 10^{-4} (see Table 1). We use **McLUSTER** to generate the initial conditions for the N -body and MOCCA codes. Models R005N750k and R005N500k have been motivated by some of the most recent observations with JWST at high redshift, that revealed dense stellar systems with effective radii of $\lesssim 1$ pc and masses of the order $10^6 M_\odot$ (Vanzella et al. 2022a; Adamo et al. 2024). Models R001N250k, R001N100k, and R0005N50k correspond to a proof of concept to show the expected evolution in a higher density regime. This work investigates compact, low-particle clusters to study massive object formation in dense stellar systems. Computational constraints limit us to smaller numbers of stars, but still allow us to explore the effect of shorter dynamical timescales.

In Fig. 1, we display the initial half-mass density ρ_h of the star cluster model, evaluated at the initial half-mass radius r_h , versus the initial star number N . We include a color bar to represent the average logarithm of the half-mass radius. In this figure, we compare the average values of different sets of simulations

Table 1. The first column lists the model names, followed by the half-mass radius in the second column, then in the third column is the initial number of stars, the fourth and fifth columns are the mass and central half density of the cluster, respectively and the last column is the absolute metallicity Z

Models	R_h [pc]	N 10^5	M [$10^5 M_\odot$]	ρ_h [$M_\odot \text{pc}^{-3}$]	Z
R005N750k	0.05	7.5	4.38	4.18×10^8	10^{-4}
R005N500k	0.05	5	2.93	2.79×10^8	10^{-4}
R001N250k	0.01	2.5	1.46	1.74×10^{10}	10^{-4}
R001N100k	0.01	1	0.58	6.92×10^9	10^{-4}
R0005N50k	0.005	0.5	0.28	2.67×10^{10}	10^{-4}

and the code used, including the direct N -body codes, shown as circle symbols in plot representing initial conditions from Portegies Zwart et al. (1999b); Fujii & Portegies Zwart (2013); Katz et al. (2015); Wang et al. (2015); Mapelli (2016); Sakurai et al. (2017); Reinoso et al. (2018b); Panamarev et al. (2019); Reinoso et al. (2020); Di Carlo et al. (2020); Rastello et al. (2021); Rizzuto et al. (2021); Banerjee (2021); Gieles et al. (2021); Vergara et al. (2021); Kamlah et al. (2022b); Rizzuto et al. (2023); Vergara et al. (2023); Arca Sedda et al. (2023, 2024a,b); Vergara et al. (2025), which are P+99, F+13, K+15, W+15, M+16, S+17, R+18, P+19, R+20, D+20, R+20, R+21, B+21, G+21, V+21, K+22, R+23, V+23, AS+23, and V+25, respectively. Simulations with Monte-Carlo codes are shown as square symbols in the plot representing initial conditions from Askar et al. (2017); Rodriguez et al. (2019); Kremer et al. (2020); Maliszewski et al. (2022); Rodriguez et al. (2022), which are A+17, R+19, K+20, M+22, and R+22, respectively. Finally hybrid N -body simulations with diamond symbols in the plot represent the initial conditions from Wang et al. (2021, 2022, 2024), which are labeled as W+21, W+22, and W+24, respectively. The latter use the PeTAAR code (Wang et al. 2020a), which is classified as a hybrid N -body code, because it combines direct particle-particle interactions with accelerated tree-based approximations. Particularly we include the following key benchmarks: the first N -body simulation with one million body, known as the DRAGON simulation, with an average density of $\rho_h \sim 10^4 M_\odot \text{pc}^{-3}$ (Wang et al. 2015); the DRAGON-II simulations by Arca Sedda et al. (2023, 2024a,b) exhibiting densities $\rho_h = 1.3 \times 10^4$ to $6.9 \times 10^5 M_\odot \text{pc}^{-3}$ for a particle range of $N = 1.2 \times 10^5 - 10^6$, with 10 – 33% of primordial binaries, and forming BHs with masses around 60 – 350 M_\odot . Additionally, Vergara et al. (2023) simulated compact clusters with equal-mass stars, reaching densities up to $10^{10} M_\odot \text{pc}^{-3}$ with fewer particles ranging from $N \sim 10^3 - 10^4$, forming massive objects of 60 – 68 000 M_\odot . The recent one-million-particle simulation by Vergara et al. (2025) achieved the highest recorded density to date $\rho_h = 6.9 \times 10^7 M_\odot \text{pc}^{-3}$, and produced an IMBH with a mass of 50 000 M_\odot . In the present work, we report simulations that reach even higher central densities, up to $\rho_h \sim 10^{10} M_\odot \text{pc}^{-3}$.

3. Results

In this section, we analyze the cluster evolution for the different models, taking into account their varying numbers of particles and half-mass radii, and thus, their densities. We investigate their stellar dynamics, stellar evolution, and VMS/BH seed formation.

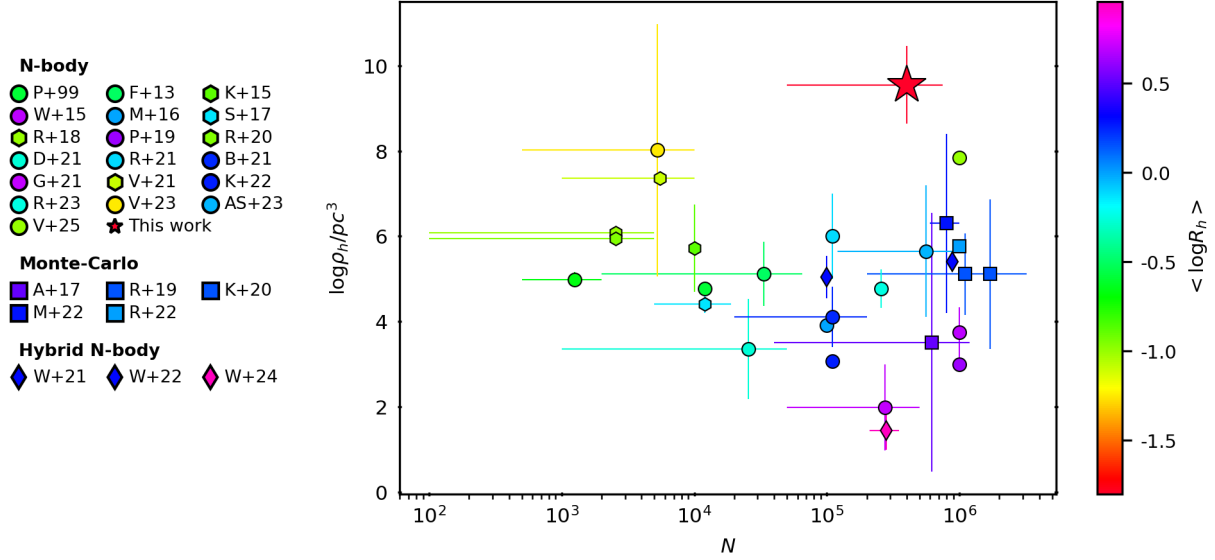


Fig. 1. Initial half-mass density ρ_h , computed at the initial half-mass radius r_h , is expressed as a function of the initial number of stars N . Figure has been reproduced from Arca Sedda et al. (2023, 2024a,b) and has been adapted to include a color bar with the logarithm of the average half-mass radius. Besides we include others simulations and the new ones presented in this paper.

3.1. Dynamical evolution of stellar clusters

In this subsection, we analyze the evolution of the cumulative mass that escapes from the star clusters, the number of collisions, and the Lagrangian radii at 90%, 50%, 30%, 10%, 5% and 1%.

The dynamics of stellar clusters are governed by key timescales, the average collision timescale (t_{coll}) which determines the frequency of stellar collisions and is expressed as $t_{coll} = \sqrt{R/GM(n\Sigma_0)^2}$ (Binney & Tremaine 2008), where R and M are the radius and the mass of the cluster, G is the gravitational constant, Σ_0 is the effective cross-section and n is the number density within the half mass radius; and the relaxation timescale (t_{rx}) which describes the time for the cluster to reach equilibrium via gravitational interactions and follows $t_{rx} = (0.1N/\ln(\gamma N))t_{cross}$, where $t_{cross} = \sqrt{R^3/GM}$, γ is the Coulomb logarithm and N the number of stars (Binney & Tremaine 2008). From an analysis of observational data of NSCs, Escala (2021) proposed that comparing relaxation and collision timescales (t_{rx} , t_{coll}) with the age of a cluster (τ) determines whether collisions drive massive central object formation. Vergara et al. (2023) tested this using equal-mass star simulations, defining a critical mass when $t_{coll} = \tau$ to quantify the transition to collision-dominated evolution, leading to a critical mass $M_{crit} = R^{7/3} (4\pi M_*/3\Sigma_0\tau G^{1/2})^{2/3}$, marking the onset of runaway stellar collisions when $M/M_{crit} \sim 0.1$.

In Fig. 2, we present the dynamical regime of stellar systems in terms of their half-mass radius and total mass. We illustrate the interplay between both key dynamical timescales, t_{coll} and t_{relax} that fall within the range $1 \text{ Myr} \leq \tau \leq 10 \text{ Gyr}$, highlighting different dynamical regimes: pink for two-body relaxation and grey for stellar collisions. The lower limit of $\tau = 1 \text{ Myr}$ corresponds approximately to the typical timescale for early cluster formation and the lifetimes of the most massive stars, while the upper limit of $\tau = 10 \text{ Gyr}$ is set by the Hubble time, representing the maximum age over which stellar systems can dynamically evolve. The grey-shaded region is where collisions are significant throughout the lifetime of the cluster, they are practically from the very beginning in post-collapse evolution. It also illus-

trates the concept of a critical mass that increases steeply with radius, meaning that compact systems are more prone to entering the collisional regime. On the other hand, the pink-shaded region is where stellar systems **are more likely to** evolve by relaxation and avoid collisions (Escala 2021; Vergara et al. 2023). The overlapping region, dark pink, where both the two-body relaxation time and the stellar collision times fall between 1 Myr and 10 Gyr, suggests that systems in this region are neither extremely dense nor extremely diffuse, but instead evolve significantly through both two-body relaxation and direct stellar collisions over cosmic timescales. The shaded pink and black areas present an asymmetry that highlights that relaxation is a more widespread and efficient process across a wide range of stellar systems, whereas frequent stellar collisions require much more compact and dense conditions.

We also include the initial half-mass radii and masses of our models (see Table 1) connected with an arrow to the final half-mass radii and masses of the respective models R005N750k, R005N500k, R001N250k, R001N100k and R0005N50k, which are denoted by yellow, cyan, orange, green, and magenta star symbols, respectively (empty for initial and full for final properties). Our models lie between the dotted lines (when t_{coll} and t_{rx} are equal to $\tau = 4 \text{ Myr}$). The models R001N250k, R001N100k, and R0005N50k fall within the collision-dominated regime. Their proximity to the dotted line indicates that they will experience several collisions, leading to the early formation ($< 4 \text{ Myr}$) of a massive central object (Escala 2021; Vergara et al. 2023). In contrast, the R005N750k and R005N500k models lie in the dark pink region. These systems are also susceptible to collisions but will proceed through a more typical relaxation process. While the models within the grey-shaded area display highly stochastic behavior, those in the dark pink region evolve in a comparatively less chaotic manner.

The expansion of a star cluster is a well known phenomenon, driven primarily by internal dynamical processes but also by external tidal forces (see e.g. Fujii & Portegies Zwart (2016)). Over time, the escape rate from the cluster increases significantly as binary interactions become more frequent, indicating that stel-

lar escapes are primarily driven by energy generated in these encounters. This gradual loss of stars, known as cluster evaporation, leads to a decrease in the mass of the cluster (see Appendix D). Additionally, binary stars can inject energy into the system through three-body encounters, further enhancing the expansion of the cluster. Our models evolve rightward and downward in parameter space as a result of expansion driven by mass loss through escapers. Despite being more compact due to computational limits, our simulated clusters host BH seeds ranging from a few thousand to tens of thousands of solar masses (see Fig. 5). Observing stellar systems that host BHs remains challenging, as the high core brightness often obscures the possible presence of a black hole. Nonetheless, a BH candidate with a mass of at least $8200 M_{\odot}$ was recently identified at the center of ω Cen, based on observations of stars moving faster than the expected central escape velocity of the cluster (Häberle et al. 2024).

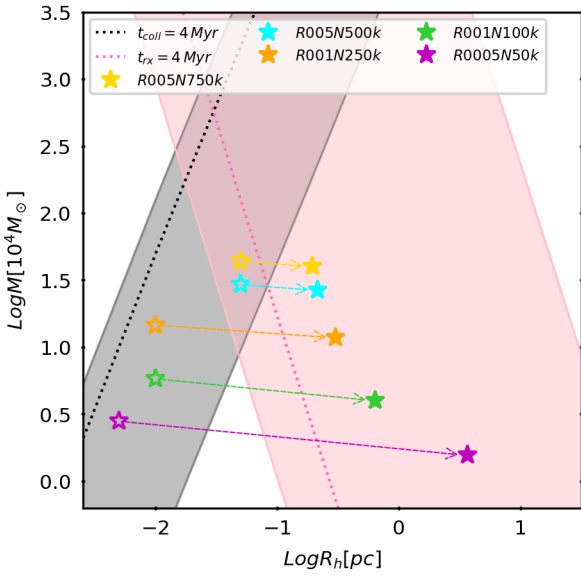


Fig. 2. The dotted lines represent when the timescales (t_{coll} and t_{rx}) are equal to $\tau = 4$ Myr. The shaded regions indicate the parameter space where the respective timescales fall within the range $1 \text{ Myr} \leq \tau \leq 10 \text{ Gyr}$, highlighting different dynamical regimes: pink for two-body relaxation and grey for stellar collisions. Our clusters R0005N50k, R001N100k, R001N250k, R005N500k, and R005N750k, evolve for 3.73, 3.81, 3.64, 3.80, 3.87 Myr, respectively. We show their initial conditions with empty symbols and the final conditions with filled symbols, connected by arrows.

In Fig. 3, we display the evolution of two models, R0005N50k and R005N750k, the densest star cluster and the most massive star cluster, respectively. We present the temporal evolution of the Lagrangian radii for models R005N750k and R0005N50k. The top panel shows the temporal evolution of model R005N750k; the Lagrangian radius at 1% shows a sharp decline at the start of the simulation due to mass segregation, followed by a decrease of the 5% after 1 Myr, while the 10% shows a slight initial decrease before it evaporates smoothly and begins to decline slightly later. The 30% and 50% radii have an initial expansion which then continues steadily until the end. In contrast, the 90% radius grows consistently throughout the simulation. The bottom panel shows that the 1% and 5% radii decrease sharply at the beginning of the simulation, while the 10% begins its decline slightly later. Eventually, all three curves over-

lap, since the VMS controls the radii; the 30% and 50% radii have an initial more rapid expansion then smoothly continue expanding to the end, while the 90% grows drastically at the beginning and then remains almost constant for the remainder of the simulation. Both models exhibit a steep initial decline in their innermost regions (1%), although in R0005N50k, the 1% and 5% curves overlap at the start of the simulation; in R005N750k, the 5% radius decreases more gradually after 1 Myr. In R005N750k, the 10% curve expands smoothly before a late decline, while in R0005N50k, it drops off earlier and merges with the innermost curves. The 30% and 50% curves expand in both cases; however, in the R0005N50k model, it is faster than in R005N750k. Finally, R0005N50k shows a more abrupt initial growth in the 90% curve, which then stabilizes, unlike the constant growth observed in R005N750k. These differences suggest that the initial conditions significantly influence the dynamical evolution of the system. Model R005N750k has a less violent behavior than model R0005N50k; this less violent process helps to retain more stars within the cluster, which is a reserve of stars that eventually can fall to the center, contributing to the growth of the VMS due to the constant stellar bombardment. On the other hand, R0005N50k presents a stochastic evolution, where several stars segregate almost intermediately to the center; however the low number of particles does not allow the VMS to be more massive.

In Fig. 4, we show the time evolution of the cumulative escaping mass normalized by the initial cluster mass (top panel) and the cumulative number of collisions involving the VMS, normalized by the initial number of stars (bottom panel) for our five cluster models; the solid lines represent the results of direct N-body simulations, while the dashed lines show the results of Monte Carlo simulations.

In the top panel, we observe that clusters with fewer particles (e.g., model R0005N50k) exhibit higher escape mass fractions compared to those with more particles (e.g., model R005N750k). These lower- N clusters are also denser, which leads to more dramatic dynamical evolution: the inner regions rapidly collapse at the beginning of the simulation, triggering multiple collisions. Additionally, enhanced three-body interactions increase the number of stars escaping from the system (see bottom panel in Fig. 3). In contrast, clusters with more particles (but lower density) show a lower ratio of cumulative escape mass normalized by the initial cluster mass, these systems exhibit a lower ratio of the number of binary collisions to the initial number of particles, thus the evaporation process is weaker (see Appendix D). The cumulative mass of escapers is $12\,371 M_{\odot}$, $17\,252 M_{\odot}$, $27\,173 M_{\odot}$, $24\,431 M_{\odot}$, and $31\,133 M_{\odot}$ in N-body simulations, and $13\,380 M_{\odot}$, $18\,888 M_{\odot}$, $44\,610 M_{\odot}$, $45\,640 M_{\odot}$, and $29\,984 M_{\odot}$ in Monte Carlo simulations for models R0005N50k, R001N100k, R001N250k, R005N500k, and R005N750k, respectively.

In the bottom panel, models R0005N50k, R001N100k and R001N250k with the smallest size ($R_h \leq 0.01 \text{ pc}$) and lowest particle number show the highest collision rate, consistent with its dense and rapidly collapsing core. Monte Carlo and N-body results agree reasonably well, though the Monte Carlo simulations tend to slightly underestimate the number of collisions (see Appendix B for details). Models R005N500k and R005N750k, representing the most massive and extended clusters, show the lowest per-star collision rates due to longer relaxation times, with similar trends in both simulation approaches. Denser clusters present higher ratios, however, since the collision counts are normalized by the initial number of stars, the ratio does not directly reflect the absolute number of collisions. The total number of collisions with VMS is 1135, 1571, 5956, 5100, 10919 in N-

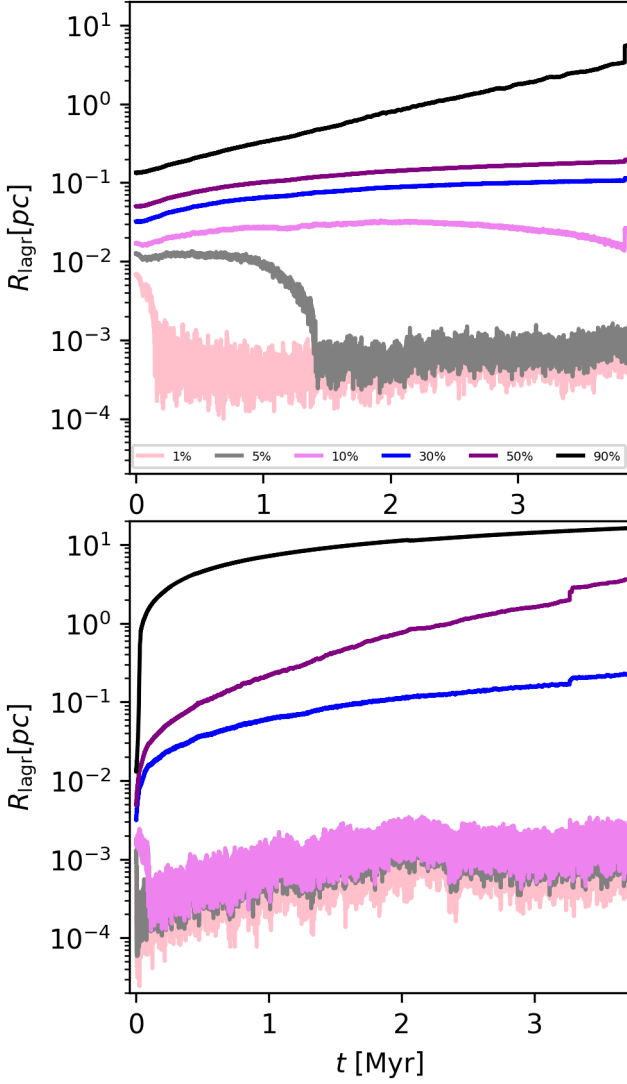


Fig. 3. Lagrangian radii calculated from the initial mass of the cluster for the 90%, 70%, 50%, 30%, 10%, and 1% of the enclosed mass of model R005N750k (top) and model R0005N50k (bottom).

body and 716, 404, 1182, 2859, 4417 in Monte Carlo simulations for models for models R0005N50k, R001N100k, R001N250k, R005N500k, and R005N750k, respectively. Although the Monte Carlo method yields fewer total collisions, these typically involve more massive stars ($> 100 M_{\odot}$), while the N -body simulations produce more frequent collisions involving lower-mass stars ($< 1 M_{\odot}$). For more discussion on this distinction, refer to Appendix C.

3.2. Black hole formation efficiency

In this subsection, we analyze the BH masses and their formation efficiency $\epsilon_{BH} = (1 + M_f/M_{BH})^{-1}$, which is defined as the fraction of mass between the final mass of the cluster and the mass of the BH mass. This efficiency quantifies the fraction of the total stellar mass available in the system that eventually ends up in the BH, through stellar collisions, making it possible to explore the transition from a star-dominated cluster ($\epsilon_{BH} \sim 0$) to a BH-dominated cluster ($\epsilon_{BH} \sim 1$) as a function of the ratio of the initial mass to the critical mass M/M_{crit} .

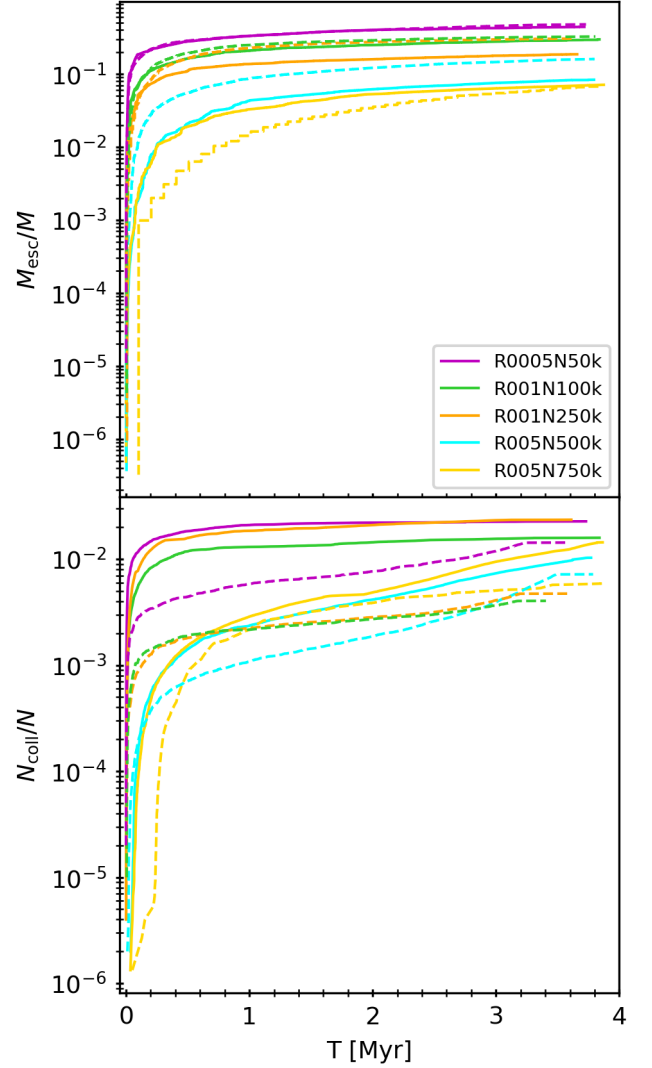


Fig. 4. Time evolution of the cumulative escaping mass normalized by the initial cluster mass (top) and the number of collisions with the most massive object normalized by the initial particle numbers (bottom). Solid lines for N -body and dashed lines for MOCCA simulations.

Fig. 5, shows the mass evolution of the VMS/BH seeds, in our five cluster models. Solid lines indicate the results from direct N -body simulations, while dashed lines represent Monte Carlo simulations. In models R005N750k and R005N500k, both simulation types show a steep increase in mass with time, with Monte Carlo results reaching slightly higher values. Model R001N250k, shows an early rapid increase in mass, with a plateau around 1 Myr for both methods, presenting a slightly higher mass in N -body simulation. Models R001N100k and R0005N50k, reach a much lower total mass, with their growth mostly flattening after $\lesssim 0.5$ Myr. The VMS forms earlier in less massive clusters, whereas in more massive clusters the VMS is more massive, its growth is prolonged because of continued stellar bombardment. The formation of the BH seeds is delayed in clusters with larger particle numbers, as the larger stellar reservoir allows the VMS to rejuvenate more frequently, postponing its collapse. All curves show a characteristic drop when the BH seed is formed, corresponding to a loss of mass 10% due to neu-

trino emission (Fryer et al. 2012; Kamlah et al. 2022a). We summarize the masses milestones for each model in Table 2.

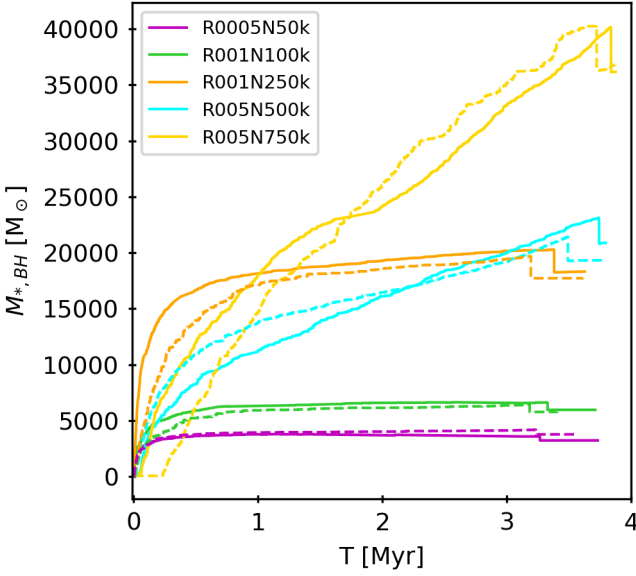


Fig. 5. Time evolution of the mass growth of VMSs that collapse into BH seeds. Solid lines for N -body and dashed lines for MOCCA simulations.

In Fig. 6, we show the BH formation efficiency (ϵ_{BH}) as a function of the ratio of the initial mass to the critical mass M/M_{crit} . The black dashed line represents an asymmetrical sigmoid function fitted to both numerical simulations and observational data collected in Vergara et al. (2024), which includes diverse stellar systems, encompassing various initial conditions, initial mass functions, and evolution scenarios. To quantify the uncertainty in our nonlinear fit, we employ a bootstrap resampling method. By repeatedly resampling the original data with replacement 1000 times and refitting the asymmetric sigmoid curve, we generate a set of fitted curves. From this set, we derive empirical confidence intervals at the uncertainties of the 1σ , 2σ , and 3σ regions, calculating the corresponding percentiles of the predicted curves at each point. These confidence bands provide a robust, nonparametric estimate of the uncertainty in the fitted model that naturally accounts for the noise and variability of the observed and simulated data collected in Vergara et al. (2024). The form of the fit is given by, $\epsilon_{BH} = (1 + \exp[-k(\log(M/M_{crit}) - x_0)])^a$, where $k = 4.63$ controls the steepness of the transition, $x_0 = 4$ sets its location, and $a = -0.1$ determines the smoothness of the function.

The efficiency starts to increase when the initial mass approaches the critical mass, i.e., $M/M_{crit} \sim 0.1$ (Vergara et al. 2024). We include our models, those with higher densities exhibit the highest BH formation efficiency, even though their BH seeds are the lightest. Since ϵ_{BH} is a function between the BH mass and the remnant stellar mass. However, systems with more particles but lower densities show a lower efficiency. However, they experience more collisions, leading to heavier BH seeds compared to denser systems. We also include the simulation from Vergara et al. (2025), which aligns well with the models presented in this work and the trend observed in Vergara et al. (2024). The density plays an important role in the onset of collisions and VMS formation; however it is also limited by the number of stars available to sink to the center, so the formation of a VMS and subsequently a BH seed is influenced by these two

parameters. In Table 3, we summarize the BH seed masses, the formation time and the BH formation efficiency (ϵ_{BH}).

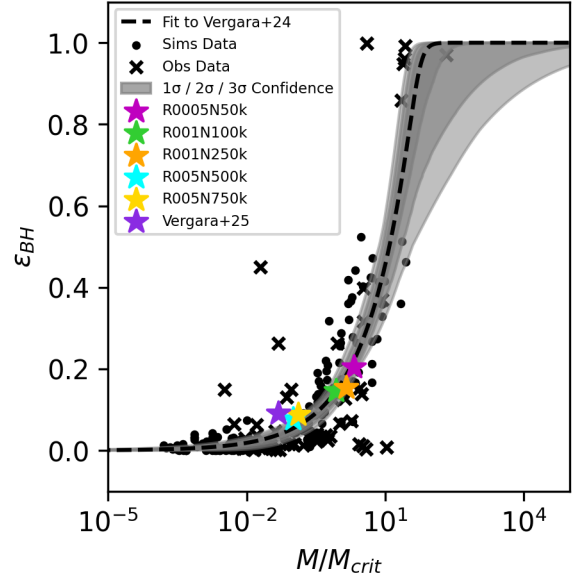


Fig. 6. BH formation efficiency as a function of the ratio of initial cluster mass to critical mass. The figure has been reproduced from Vergara et al. (2024); we fit an asymmetrical sigmoid function, represented by the black dashed line. The shaded grey bands represent the confidence intervals estimated by bootstrap resampling: the darker, middle, and lighter grey bands correspond to the 1σ , 2σ , and 3σ uncertainty regions. These intervals quantify the uncertainty in the fitted curve, arising from data variability. We add the simulation from Vergara et al. (2025) and the simulations from this work.

3.3. Comparison with JWST observations

In this subsection, we compare our results with observational data including Young Star Clusters (YSCs) (Brown & Gnedin 2021), as well as recent observations with JWST of YMCs (Vanzella et al. 2022b,a,c, 2023; Mowla et al. 2024; Adamo et al. 2024).

On the left side of Fig. 7, we show the effective radii and masses of YSCs which are denoted by grey crosses, while recent observations of YMCs with JWST are represented by blue symbols with black edges. YSCs span a wider range of the parameter space (see Brown & Gnedin (2021)), but here we focus on those with masses between $10^4 M_\odot$ and $10^6 M_\odot$ and effective radii from ~ 0.1 pc to > 10 pc. YMCs have masses between 10^5 and $10^8 M_\odot$ and effective radii from < 1 to > 10 pc. We compute the effective radii at the end of the simulations and also include our previous work from Vergara et al. (2025). Our simulations (star symbols) fall into the mass range of 10^4 and $10^6 M_\odot$, matching both the YSCs and the YMCs. The final effective radii range between ~ 0.1 pc and 1 pc; our simulated cluster lies further to the left than the observations. However, our simulations are very short, around 4 Myr, so they do not have enough time to expand and thus move to the right in the plot. In particular, the varying shades of the grey crosses indicate their ages, with lighter colors representing younger ages and darker colors indicating older ones. The most massive YSCs typically exhibit smaller radii, whereas younger clusters tend to appear at the bottom, characterized by lower masses and larger radii (see Brown & Gnedin (2021), for details). This suggests that the most mas-

Table 2. The first column lists the model names, followed by columns showing the times ($\tau_{VMS, 1k}$, $\tau_{VMS, 5k}$, $\tau_{VMS, 10k}$, $\tau_{VMS, 20k}$, $\tau_{VMS, 30k}$, $\tau_{VMS, 40k}$) at which the VMS reach certain mass milestones $\sim 1000, 5000, 10\,000, 20\,000, 30\,000, 40\,000\,M_{\odot}$, respectively. MOCCA results are shown in round brackets next to N -body results. A horizontal dash indicates that the VMS ended its life before reaching the corresponding mass milestone.

Models	$\tau_{VMS, 1k}$ [Myr]	$\tau_{VMS, 5k}$ [Myr]	$\tau_{VMS, 10k}$ [Myr]	$\tau_{VMS, 20k}$ [Myr]	$\tau_{VMS, 30k}$ [Myr]	$\tau_{VMS, 40k}$ [Myr]
R005N750k	0.069 (0.27)	0.16 (0.45)	0.38 (0.68)	1.16 (1.44)	2.69 (2.31)	3.81 (3.58)
R005N500k	0.063 (0.03)	0.20 (0.11)	0.74 (0.41)	3.01 (3.18)	– (–)	– (–)
R001N250k	0.0051 (0.02)	0.022 (0.1)	0.066 (0.25)	2.78 (–)	– (–)	– (–)
R001N100k	0.0083 (0.02)	0.21 (0.4)	– (–)	– (–)	– (–)	– (–)
R0005N50k	0.0031 (0.01)	– (–)	– (–)	– (–)	– (–)	– (–)

Table 3. The first column lists the model names, followed by the mass of the BH seed, then the time of BH formation, and finally the BH formation efficiency. MOCCA results are shown in round brackets next to N -body results.

Models	M_{BH} [$10^3 M_{\odot}$]	τ_{BH} [Myr]	ϵ_{BH}
R005N750k	36.1 (36.2)	3.83 (3.72)	8.87 (8.87) %
R005N500k	20.8 (19.2)	3.74 (3.48)	7.74 (7.80) %
R001N250k	18.3 (17.7)	3.37 (3.19)	15.39 (17.45) %
R001N100k	5.95 (5.76)	3.32 (3.18)	14.58 (14.69) %
R0005N50k	3.22 (3.75)	3.26 (3.23)	20.51 (25.51) %

sive clusters expand more slowly, which is consistent with our simulations (see Fig. 2).

On the right side of Fig. 7, we present the stellar surface densities and masses for our simulated clusters, alongside those from Vergara et al. (2025). The simulated clusters span surface densities from approximately 10^3 – $10^6\,M_{\odot}\,\text{pc}^{-2}$, similar to those observed in the local Universe, like YSCs, as well as YMCs at both low and high redshift, often regardless of their higher masses (e.g., Adamo et al. 2024). In our simulations, the more massive clusters have both higher surface densities and slightly older ages, which is consistent with trends in the observed YSC populations (Brown & Gnedin 2021). Observationally, a similar pattern emerges for YMCs; lower-mass clusters are typically younger (ages ~ 3 – 4 Myr), as seen at $z \sim 8$ in Mowla et al. (2024), while the most compact and massive clusters are generally somewhat older, with ages up to about 36 Myr at $z \sim 10$ (Adamo et al. 2024). The YMCs studied by Vanzella et al. (2022b,a, 2023) at redshifts $z \sim 2$ – 6 show a wide range of masses and ages, from 1 to 30 Myr, further illustrating the diversity of cluster properties in the early Universe.

Overall, our simulations reproduce the observed trend that more massive and older clusters tend to have higher stellar surface densities, although the absolute values for YMCs can be substantially higher than those of lower-mass YSCs. This highlights the importance of both the cluster mass and evolutionary stage in shaping the structural properties of star clusters across cosmic time.

3.4. Expected BH masses in YMCs detected via JWST

Many of the observed YMCs have effective radii of a few pc and ages ranging from a few to several tens of Myr. Although they are massive stellar systems, it remains unclear whether their initial central densities were high enough to trigger efficient BH formation. While it is generally assumed that clusters were more compact at birth, the degree of this initial compactness remains uncertain. However, the critical mass exhibits a nonlinear depen-

dence on cluster size and density: compact clusters reach this threshold at lower total masses. Thus, NSCs or YMCs can lie well near the M_{crit} region (see Fig. 2), making them prime environments for collisional evolution and central object formation.

YMCs, though younger and potentially more transient than NSCs, can still reach extremely high densities shortly after formation (Lahén et al. 2025). If they are compact enough, the early phases of their evolution may fall within the regime where $t_{\text{coll}} < t_{\text{rx}} < \tau$. This opens a window during which massive stars can undergo collisions before they evolve off the main sequence, potentially forming exotic objects such as VMSs or heavy BH seeds. This makes M_{crit} a predictive tool not only for understanding cluster evolution, but also for identifying which systems might contribute to the formation of gravitational wave sources or seed BHs.

Based on the relationship between BH formation efficiency and the ratio of star cluster mass to critical mass, we estimate the expected minimum mass of massive BHs in these YMCs, under the assumption of a collision-driven formation scenario. In an initially more conservative estimate, we adopt the current mass and radius of the cluster to evaluate the initial to critical mass ratio, without accounting for potential early compactness or the presence of gas. The derived BH mass should therefore be considered a lower limit from the standpoint of stellar dynamics. Higher actual BH masses are not excluded, as additional growth could happen via accretion. In a more optimistic yet still realistic, scenario, we assume that the clusters were initially more compact, as suggested by the scaling relation $r_h \propto t^{2/3}$ (Fujii & Portegies Zwart 2016)². This would increase the stellar collision rate and thus the likelihood of forming more massive BHs. However, as noted above, it is not guaranteed that all of the observed clusters were compact enough to meet the conditions required by these models and specific properties of the clusters such as a higher binary fraction could also lead to a difference in their evolution. Furthermore, we neglect here the potential role of gas, which could enhance both the conditions for BH formation and subsequent BH growth through accretion.

Fig. 8 shows the expected BH mass as a function of the stellar mass for the sources in the sample of Vanzella et al. (2022a,b, 2023); Adamo et al. (2024); Mowla et al. (2024). The more conservative prediction is shown on the top panel, while the more optimistic one is shown in the bottom panel. As the sample includes star clusters with different ratios of initial over critical masses, it includes both clusters where we expect high efficiencies of up to 1%, but also clusters with low efficiencies of order 0.01%. This is in the conservative case, while in the more optimistic case we expect efficiencies up to 10%.

² This relation holds for isolated clusters without mass loss (Giersz & Heggie 1996, 1997). For tidally limited clusters, post core-collapse expansion can still be approximated by a power law $r_h \propto t^{(2-\mu)/3}$, where the index μ depends on the rate of mass loss.

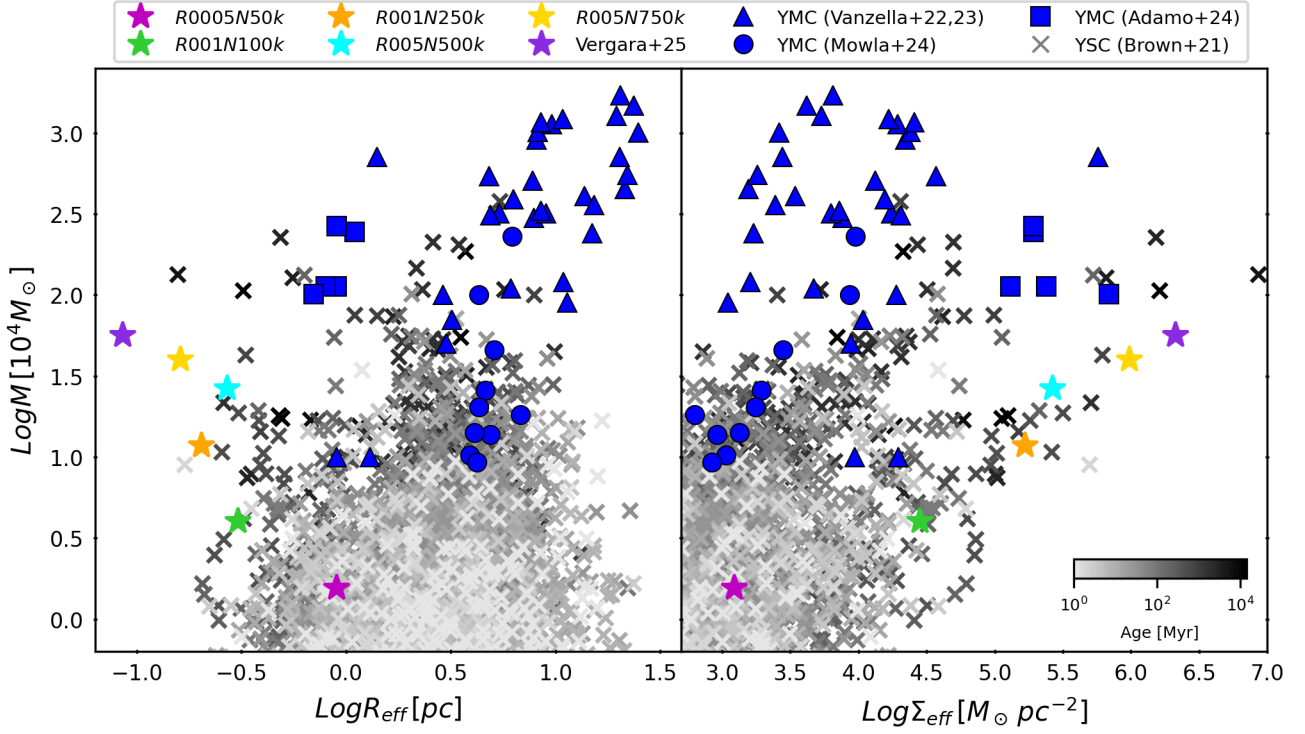


Fig. 7. The final masses of our simulated clusters, along with the simulated cluster from Vergara et al. (2025), are shown as star symbols. The current masses of YSCs from Brown & Gnedin (2021) are also included, with the colorbar indicating their ages. Recent JWST observations of YMCs (Vanzella et al. 2022b,a, 2023; Mowla et al. 2024; Adamo et al. 2024) are shown with blue symbols, all plotted against the effective radius (left) and surface density (right).

We find a relation between the mass of the cluster and the predicted mass of the BH that follows the shape of $\log(M_{\text{BH}}/M_\odot) = -2 + 0.88 \log(M/M_\odot)$, for the conservative case, and other with the shape of $\log(M_{\text{BH}}/M_\odot) = -0.76 + 0.76 \log(M/M_\odot)$, for the optimistic one. We expect that these predictions could be tested through a cross-correlation of the positions of the known sources with current and future X-ray data, which may lead to detections or at least upper limits for the BH masses that could be present within these sources. We also suggest that the presence of such a population of massive BHs at early times is likely to lead to relevant observables for the Laser Interferometer Space Antenna (LISA).

4. Summary and conclusions

We present simulations of the densest stellar clusters to date using `NBODY6++GPU` and the `MOCCA` code. Our models include the latest updates for stellar radius evolution and close encounter prescriptions (see Vergara et al. 2025). We have also updated the stellar rejuvenation treatment to ensure that when a VMS collides with a less massive star, its age does not change dramatically (see appendix A for details). Wind prescriptions follow Vink et al. (2001); Vink & de Koter (2002, 2005); Belczynski et al. (2010), with the helium-burning phases modeled using luminosity-dependent winds (Sander et al. 2020).

Our models represent stellar clusters with high density, and show BH seed formation through the purely collisional channel in a short period of time. Clusters with a higher initial number of stars experience more collisions, which can lead to the formation of more massive objects (e.g., models R005N750k and R005N500k). However, clusters with higher densities form massive objects more quickly (e.g., models R0005N50k and

R001N250k). Clusters with more particles but lower densities undergo delayed core collapse and contain a larger reservoir of relatively massive stars that can migrate inward due to mass segregation. This results in more collisions over longer timescales, allowing the VMS to be repeatedly rejuvenated through mergers and postponing its collapse into a BH seed. In contrast, high-density clusters with fewer particles experience faster core collapse, triggering earlier collisions and rapid VMS growth. The VMS in these systems quickly increases its cross-section, further enhancing the collision rate. However, the stellar reservoir is depleted sooner, leading to the earlier collapse of the VMS into a BH seed. Overall, our results show that the formation and evolution of VMSs (and their subsequent collapse into BH seeds) depend on both the cluster’s density and its number of stars. Higher densities accelerate VMS formation, while a larger number of stars increases the eventual VMS mass. The timing of BH seed formation is regulated by the number of collisions that rejuvenate the VMS, thus, clusters with more stars form BH seeds later. Recent studies also indicate that mass loss in VMSs is highly sensitive to both the mass distribution of the colliding stars and the structural evolution of the VMS itself (Ramírez-Galeano et al. 2025).

Dense stellar clusters form in environments with low metallicity and high gas density (Fukushima & Yajima 2023), where radiative pressure is insufficient to prevent collapse. This leads to an extremely high star formation efficiency (SFE) of around 80% (Menon et al. 2023; Somerville et al. 2025). Mergers of gas-rich dwarf galaxies at high redshift have also been proposed as a viable pathway for assembling massive, compact stellar systems (Renaud et al. 2015; Lahén et al. 2020b,a; Lahén et al. 2025). Recent simulations suggest that, in such environments, the merger of star clusters hosting massive BHs can lead to the rapid forma-

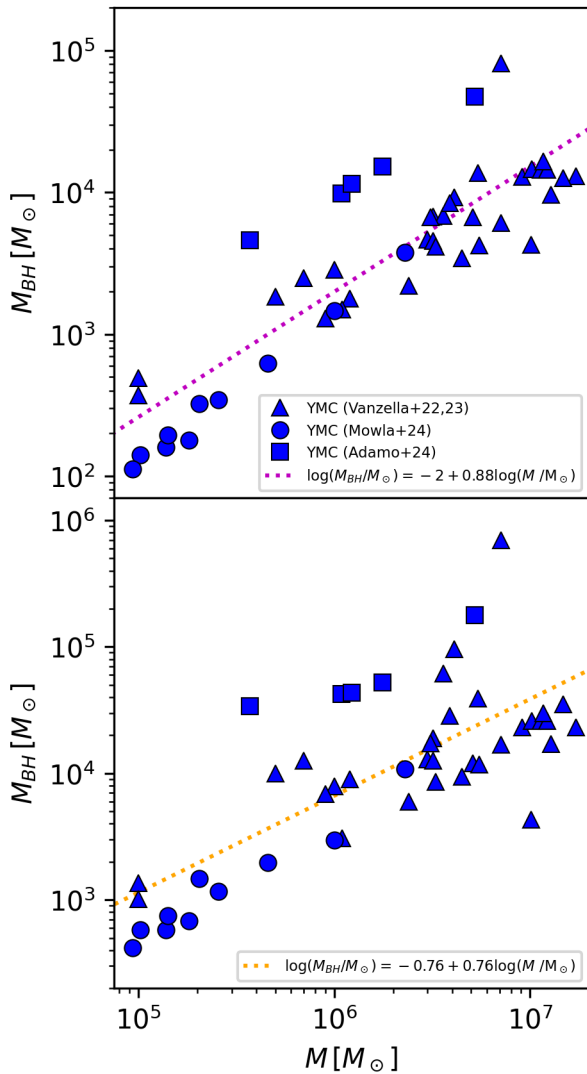


Fig. 8. Expected BH masses within YMCs against their current stellar mass. The top panel shows the conservative case, while the bottom panel shows the optimistic one.

tion of hard binary BH systems. These binaries interact strongly with surrounding stars and stellar-mass BHs, driving substantial ejection of both stellar and compact objects (Souvatzis et al. 2025). Repeated ejections during and after cluster mergers can significantly reduce the final mass of the resulting cluster. These extremely dense stellar clusters are also ideal sites for the formation of supermassive stars through runaway collisions within their cores (Charbonnel et al. 2023).

Our models exhibit stellar collision rates much higher than those typically found in globular cluster simulations, such as the DRAGON-II runs (Arca Sedda et al. 2023, 2024a,b). In our simulations, the timescale for collisions is shorter than the thermal timescale of the VMS, preventing the star from reaching thermal equilibrium. This can drive radial expansion, increase the star’s cross-section, and further enhance the collision rate. In addition, this process rejuvenates the VMS, delaying the formation of a BH seed. The thermodynamic state of such a VMS remains poorly understood. Mass loss could be driven by stellar winds or by stellar mergers (Dale & Davies 2006), which also provide an additional enrichment pathway by ejecting processed material into the interstellar medium (Gieles et al. 2018; Wang et al.

2020b). However, the assumed rapid thermal recovery after each collision allows mass growth to outpace wind-driven mass loss.

VMS formation through runaway stellar collisions in dense star clusters was first proposed analytically by Begelman & Rees (1978); Rees (1984), and Lee (1987). Subsequent studies employed Fokker–Planck and Monte Carlo methods (Quinlan & Shapiro 1990; Gürkan et al. 2004; Freitag et al. 2006b,a; Giersz et al. 2015) and direct N -body simulations (Vergara et al. 2023, 2025; Rantala & Naab 2025; Rantala et al. 2025). In this study, dense stellar systems allow us to explore their dynamics and their ability to form VMSs in a short time due to the constant bombardment of stars sinking towards the center. The deep gravitational potential presented in these stellar systems leads to the onset of collisions that quickly trigger the formation of a VMS $\gtrsim 1000 M_\odot$ in less than 0.1 Myr.

For the YMCs observed with JWST, the collision-based formation scenario implies BH masses in the range of 10^2 – $10^5 M_\odot$ within these clusters. In our analysis, we considered both a conservative scenario (assuming the cluster masses and radii remain constant over time) and a more realistic scenario in which clusters undergo expansion, increasing the likelihood of forming massive objects due to higher initial densities. The numbers derived here are likely lower limits, as we did not account for the possible effects of gas. However, for more extended clusters, it is possible that massive object formation could be avoided in some cases. Moreover, the clusters observed with JWST are those that survived for a considerable period of time, while the densest clusters may have already collapsed and formed a massive BH at an earlier stage, as discussed by Escala (2021). The presence of these BHs could be confirmed or constrained with current and future X-ray observations. We also note that, while it is computationally challenging to model systems like the observed LRDs, their compactness naturally favors the collision-driven formation channel. It has been shown that the LRDs can have radii of 10 pc with core densities of the order of $10^8 M_\odot \text{pc}^{-3}$; note that this represents an upper and lower limit, respectively (Guia et al. 2024). Here we considered clusters with similar and higher central densities, but with smaller radii (and fewer particles), as otherwise due to computational limitations it is not feasible to explore these high densities.

TDEs, occurring when a star is torn apart by an IMBH’s tidal forces, produce luminous flares and provide insights into BH growth (Stone & Metzger 2016; Ryu et al. 2020c,b,a; Stone et al. 2020), which are particularly important for understanding LRD emissions (Bellovary 2025). Extreme mass ratio inspirals (EMRIs), in which stellar-mass BHs or neutron stars spiral into IMBHs via gravitational wave (GW) emission, are driven by dynamical friction and relativistic effects (Hills & Bender 1995; Broggi et al. 2022, 2024). Our models indicate rapid BH seed formation through runaway stellar collisions, suggesting EMRIs could occur earlier in cosmic history than predicted. Multimessenger astronomy enables testing these theories: TDE flares are observed by the Hubble Space Telescope (HST) (Leloudas et al. 2016) and Neil Gehrels Swift Observatory (Swift) (Brown et al. 2016), while GW detectors (LIGO/ Virgo/ KAGRA) (Abbott et al. 2024) and future missions ((LISA) (Amaro-Seoane et al. 2017; McCaffrey et al. 2025), and Einstein Telescope (ET) (Punturo et al. 2010)) target compact mergers and EMRIs.

Recent JWST observations of high-redshift galaxies have revealed unexpectedly high nitrogen abundances and elevated N/O ratios (Tacchella et al. 2023; Nagele & Umeda 2023; Maiolino et al. 2024; Larson et al. 2023; Marques-Chaves et al. 2024; Naidu et al. 2025), a phenomenon that standard chemical evolution models struggle to explain (Cameron et al. 2023). While typ-

ical models predict low N/O ratios in young, low-metallicity systems (since nitrogen production is dominated by massive stars on longer timescales) the presence of VMSs offers a compelling solution. VMSs can rapidly enrich the interstellar medium with nitrogen through their strong winds and unique nucleosynthetic pathways, producing the high N/O ratios observed even in the early Universe (Charbonnel et al. 2023). Incorporating VMSs into chemical evolution models allows both the amount and timing of nitrogen enrichment to better match observations, making them a key factor in understanding the chemical signatures of young, high-redshift stellar populations.

Acknowledgements. MCV acknowledges funding through ANID (Doctorado acuerdo bilateral DAAD/62210038) and DAAD (funding program number 57600326). MCV acknowledges the International Max Planck Research School for Astronomy and Cosmic Physics at the University of Heidelberg (IMPRS-HD). AA acknowledges support for this paper from project No. 2021/43/P/ST9/03167 co-funded by the Polish National Science Center (NCN) and the European Union Framework Programme for Research and Innovation Horizon 2020 under the Marie Skłodowska-Curie grant agreement No. 945339. For the purpose of Open Access, the authors have applied for a CC-BY public copyright license to any Author Accepted Manuscript (AAM) version arising from this submission. RS acknowledges NAOC International Cooperation Office for its support in 2023, 2024, and 2025, and the support by the National Science Foundation of China (NSFC) under grant No. 12473017. This research was supported in part by grant NSF PHY-2309135 to the Kavli Institute for Theoretical Physics (KITP). FFD and RS acknowledge support by the German Science Foundation (DFG, project Sp 345/24-1). MAS acknowledges funding from the European Union's Horizon 2020 research and innovation programme under the Marie Skłodowska-Curie grant agreement No. 101025436 (project GRACE-BH, PI: Manuel Arca Sedda). MAS acknowledges financial support from the MERAC foundation. DRGS gratefully acknowledges support by the ANID BASAL project FB21003 and ANID QUIMAL220002. DRGS thanks for funding via the Alexander von Humboldt - Foundation, Bonn, Germany. AE acknowledges financial support from the Center for Astrophysics and Associated Technologies CATA (FB210003). MG was supported by the Polish National Science Center (NCN) through the grant 2021/41/B/ST9/01191. Computations were performed on the HPC system Raven at the Max Planck Computing and Data Facility, and we also acknowledge the Gauss Centre for Supercomputing e.V. for computing time through the John von Neumann Institute for Computing (NIC) on the GCS Supercomputer JUWELS Booster at Jülich Supercomputing Centre (JSC). We also acknowledge A. Sander and his team for helpful comments.

Data Availability

The underlying data, including the initial model used in this work, as well as the output and diagnostic files from both the Nbody6++GPU and MOCCA simulations, will be shared on reasonable request.

References

Abbott, R., Abe, H., Acernese, F., et al. 2024, *ApJ*, 966, 137
 Adamo, A., Bradley, L. D., Vanzella, E., et al. 2024, arXiv e-prints, 22
 Ahmad, A. & Cohen, L. 1973, *Journal of Computational Physics*, 12, 389
 Akins, H. B., Casey, C. M., Berg, D. A., et al. 2025, *ApJ*, 980, L29
 Alister Seguel, P. J., Schleicher, D. R. G., Boekholt, T. C. N., Fellhauer, M., & Klessen, R. S. 2020, *MNRAS*, 493, 2352
 Amaro-Seoane, P., Audley, H., Babak, S., et al. 2017, arXiv e-prints, arXiv:1702.00786
 Arca Sedda, M., Kamlah, A. W. H., Spurzem, R., et al. 2024a, *MNRAS*, 528, 5119
 Arca Sedda, M., Kamlah, A. W. H., Spurzem, R., et al. 2024b, *MNRAS*, 528, 5140
 Arca Sedda, M., Mapelli, M., Benacquista, M., & Spera, M. 2023, *MNRAS*, 520, 5259
 Askar, A., Szkudlarek, M., Gondek-Rosińska, D., Giersz, M., & Bulik, T. 2017, *MNRAS*, 464, L36
 Bamber, J., Shapiro, S. L., Ruiz, M., & Tsokaros, A. 2025, arXiv e-prints, arXiv:2505.01495
 Banerjee, S. 2021, *MNRAS*, 500, 3002
 Banerjee, S., Belczynski, K., Fryer, C. L., et al. 2020, *A&A*, 639, A41
 Begelman, M. C. 2010, *MNRAS*, 402, 673

Begelman, M. C. & Rees, M. J. 1978, *MNRAS*, 185, 847
 Begelman, M. C., Volonteri, M., & Rees, M. J. 2006, *MNRAS*, 370, 289
 Belczynski, K., Bulik, T., Fryer, C. L., et al. 2010, *ApJ*, 714, 1217
 Bellovary, J. 2025, *ApJ*, 984, L55
 Binney, J. & Tremaine, S. 2008, *Galactic Dynamics: Second Edition*
 Bond, J. R., Arnett, W. D., & Carr, B. J. 1984, *ApJ*, 280, 825
 Bouwens, R. J., Illingworth, G. D., González, V., et al. 2010, *ApJ*, 725, 1587
 Broggi, L., Bortolas, E., Bonetti, M., Sesana, A., & Dotti, M. 2022, *MNRAS*, 514, 3270
 Broggi, L., Stone, N. C., Ryu, T., et al. 2024, arXiv e-prints, arXiv:2404.05786
 Brown, G. & Gnedin, O. Y. 2021, *MNRAS*, 508, 5935
 Brown, P. J., Yang, Y., Cooke, J., et al. 2016, *ApJ*, 828, 3
 Cameron, A. J., Katz, H., Rey, M. P., & Saxena, A. 2023, *MNRAS*, 523, 3516
 Charbonnel, C., Schaerer, D., Prantzos, N., et al. 2023, *A&A*, 673, L7
 Chon, S. & Omukai, K. 2024, arXiv e-prints, arXiv:2412.14900
 Dale, J. E. & Davies, M. B. 2006, *MNRAS*, 366, 1424
 Di Carlo, U. N., Mapelli, M., Bouffanais, Y., et al. 2020, *MNRAS*, 497, 1043
 Escala, A. 2021, *ApJ*, 908, 57
 Fregeau, J. M., Cheung, P., Portegies Zwart, S. F., & Rasio, F. A. 2004, *MNRAS*, 352, 1
 Freitag, M., Gürkan, M. A., & Rasio, F. A. 2006a, *MNRAS*, 368, 141
 Freitag, M., Rasio, F. A., & Baumgardt, H. 2006b, *MNRAS*, 368, 121
 Fryer, C. L., Belczynski, K., Wiktorowicz, G., et al. 2012, *ApJ*, 749, 91
 Fujii, M. S. & Portegies Zwart, S. 2013, *MNRAS*, 430, 1018
 Fujii, M. S. & Portegies Zwart, S. 2016, *ApJ*, 817, 4
 Fukushima, H. & Yajima, H. 2023, *MNRAS*, 524, 1422
 Furtak, L. J., Labbé, I., Zitrin, A., et al. 2024, *Nature*, 628, 57
 Gaete, B., Schleicher, D. R. G., Lupi, A., et al. 2024, arXiv e-prints, arXiv:2406.13072
 Gieles, M., Charbonnel, C., Krause, M. G. H., et al. 2018, *MNRAS*, 478, 2461
 Gieles, M., Erkal, D., Antonini, F., Balbinot, E., & Peñarrubia, J. 2021, *Nature Astronomy*, 5, 957
 Giersz, M. 2001, *MNRAS*, 324, 218
 Giersz, M. & Heggie, D. C. 1996, *MNRAS*, 279, 1037
 Giersz, M. & Heggie, D. C. 1997, *MNRAS*, 286, 709
 Giersz, M., Heggie, D. C., & Hurley, J. R. 2008, *MNRAS*, 388, 429
 Giersz, M., Heggie, D. C., Hurley, J. R., & Hypki, A. 2013, *MNRAS*, 431, 2184
 Giersz, M., Leigh, N., Hypki, A., Lützgendorf, N., & Askar, A. 2015, *MNRAS*, 454, 3150
 Giesers, B., Dreizler, S., Husser, T.-O., et al. 2018, *MNRAS*, 475, L15
 Glebbeek, E., Pols, O. R., & Hurley, J. R. 2008, *A&A*, 488, 1007
 Goulding, A. D., Greene, J. E., Setton, D. J., et al. 2023, *ApJ*, 955, L24
 Greene, J. E., Labbe, I., Goulding, A. D., et al. 2024, *ApJ*, 964, 39
 Guia, C. A., Pacucci, F., & Kocevski, D. D. 2024, *Research Notes of the American Astronomical Society*, 8, 207
 Gürkan, M. A., Freitag, M., & Rasio, F. A. 2004, *ApJ*, 604, 632
 Häberle, M., Neumayer, N., Seth, A., et al. 2024, *Nature*, 631, 285
 Heggie, D. C. 2014, *MNRAS*, 445, 3435
 Hénon, M. 1971, *Ap&SS*, 13, 284
 Hils, D. & Bender, P. L. 1995, *ApJ*, 445, L7
 Hurley, J. R., Pols, O. R., Aarseth, S. J., & Tout, C. A. 2005, *MNRAS*, 363, 293
 Hurley, J. R., Pols, O. R., & Tout, C. A. 2000, *MNRAS*, 315, 543
 Hurley, J. R., Shara, M. M., & Tout, C. A. 2002, in *Astronomical Society of the Pacific Conference Series*, Vol. 279, *Exotic Stars as Challenges to Evolution*, ed. C. A. Tout & W. van Hamme, 115
 Hut, P., Makino, J., & McMillan, S. 1995, *ApJL*, 443, L93
 Hypki, A. & Giersz, M. 2013, *MNRAS*, 429, 1221
 Juodžbalis, I., Maiolino, R., Baker, W. M., et al. 2024, *Nature*, 636, 594
 Kamlah, A. W. H., Leveque, A., Spurzem, R., et al. 2022a, *Monthly Notices of the Royal Astronomical Society*, 511, 4060
 Kamlah, A. W. H., Spurzem, R., Berczik, P., et al. 2022b, *Monthly Notices of the Royal Astronomical Society*, 516, 3266
 Katz, H., Sijacki, D., & Haehnelt, M. G. 2015, *MNRAS*, 451, 2352
 King, I. R., Hedemann, Edmund, J., Hodge, S. M., & White, R. E. 1968, *AJ*, 73, 456
 Kokorev, V., Caputi, K. I., Greene, J. E., et al. 2024, *ApJ*, 968, 38
 Kremer, K., Ye, C. S., Rui, N. Z., et al. 2020, *ApJS*, 247, 48
 Kroupa, P. 2001, *MNRAS*, 322, 231
 Kroupa, P., Subr, L., Jerabkova, T., & Wang, L. 2020, *MNRAS*, 498, 5652
 Lahén, N., Naab, T., Johansson, P. H., et al. 2020a, *The Astrophysical Journal*, 904, 71
 Lahén, N., Naab, T., Johansson, P. H., et al. 2020b, *The Astrophysical Journal*, 891, 2
 Lahén, N., Naab, T., Rantala, A., & Partmann, C. 2025, arXiv e-prints, arXiv:2504.18620
 Larson, R. L., Finkelstein, S. L., Kocevski, D. D., et al. 2023, *ApJ*, 953, L29
 Lee, H. M. 1987, *ApJ*, 319, 801
 Leloudas, G., Fraser, M., Stone, N. C., et al. 2016, *Nature Astronomy*, 1, 0002
 Liempi, M., Schleicher, D. R. G., Benson, A., Escala, A., & Vergara, M. C. 2025, *A&A*, 694, A42

- Lodato, G. & Natarajan, P. 2006, *MNRAS*, 371, 1813
 Loeb, A. & Rasio, F. A. 1994, *ApJ*, 432, 52
 Lupi, A., Colpi, M., Devecchi, B., Galanti, G., & Volonteri, M. 2014, *MNRAS*, 442, 3616
 Madau, P. & Rees, M. J. 2001, *ApJ*, 551, L27
 Madrid, J. P., Leigh, N. W. C., Hurley, J. R., & Giersz, M. 2017, *MNRAS*, 470, 1729
 Maiolino, R., Scholtz, J., Witstok, J., et al. 2024, *Nature*, 627, 59
 Makino, J. 1999, *Journal of Computational Physics*, 151, 910
 Makino, J. & Aarseth, S. J. 1992, *PASJ*, 44, 141
 Maliszewski, K., Giersz, M., Gondek-Rosinska, D., Askar, A., & Hypki, A. 2022, *MNRAS*.tmp [arXiv:2111.09223]
 Mapelli, M. 2016, *MNRAS*, 459, 3432
 Marques-Chaves, R., Schaerer, D., Kuruvanthodi, A., et al. 2024, *A&A*, 681, A30
 Matthee, J., Naidu, R. P., Brammer, G., et al. 2024, *ApJ*, 963, 129
 McCaffrey, J., Regan, J., Smith, B., et al. 2025, *The Open Journal of Astrophysics*, 8, 11
 McMillan, S. L. W. 1986, *The Vectorization of Small-N Integrators*, ed. P. Hut & S. L. W. McMillan, Vol. 267 (Springer), 156
 Menon, S. H., Federath, C., & Krumholz, M. R. 2023, *MNRAS*, 521, 5160
 Mestichelli, B., Mapelli, M., Tornamenti, S., et al. 2024, *A&A*, 690, A106
 Mikkola, S. & Aarseth, S. J. 1990, *Celestial Mechanics and Dynamical Astronomy*, 47, 375
 Mikkola, S. & Aarseth, S. J. 1993, *Celestial Mechanics and Dynamical Astronomy*, 57, 439
 Mowla, L., Iyer, K., Asada, Y., et al. 2024, *Nature*, 636, 332
 Nagele, C. & Umeda, H. 2023, *ApJ*, 949, L16
 Naidu, R. P., Oesch, P. A., Brammer, G., et al. 2025, arXiv e-prints, arXiv:2505.11263
 Nandal, D., Sibony, Y., & Tsiatsiou, S. 2024, *A&A*, 688, A142
 Napolitano, L., Castellano, M., Pentericci, L., et al. 2024, arXiv e-prints, arXiv:2410.18763
 Omukai, K. & Nishi, R. 1998, *ApJ*, 508, 141
 Panamarev, T., Just, A., Spurzem, R., et al. 2019, *MNRAS*, 484, 3279
 Portegies Zwart, S. F., Baumgardt, H., Hut, P., Makino, J., & McMillan, S. L. W. 2004, *Nature*, 428, 724
 Portegies Zwart, S. F., Makino, J., McMillan, S. L. W., & Hut, P. 1999a, *A&A*, 348, 117
 Portegies Zwart, S. F., Makino, J., McMillan, S. L. W., & Hut, P. 1999b, *A&A*, 348, 117
 Portegies Zwart, S. F. & McMillan, S. L. W. 2002, *ApJ*, 576, 899
 Punturo, M., Abernathy, M., Acernese, F., et al. 2010, *Classical and Quantum Gravity*, 27, 194002
 Quinlan, G. D. & Shapiro, S. L. 1990, *ApJ*, 356, 483
 Ramírez-Galeano, L., Charbonnel, C., Fragos, T., et al. 2025, arXiv e-prints, arXiv:2506.12132
 Rantala, A., Lahén, N., Naab, T., Escobar, G. J., & Iorio, G. 2025, arXiv e-prints, arXiv:2506.04330
 Rantala, A. & Naab, T. 2025, arXiv e-prints, arXiv:2503.21879
 Rastello, S., Mapelli, M., Di Carlo, U. N., et al. 2021, *MNRAS*, 507, 3612
 Rees, M. J. 1978, *The Observatory*, 98, 210
 Rees, M. J. 1984, *ARA&A*, 22, 471
 Reinoso, B., Latif, M. A., & Schleicher, D. R. G. 2025, arXiv e-prints, arXiv:2503.20415
 Reinoso, B., Schleicher, D. R. G., Fellhauer, M., Klessen, R. S., & Boekholt, T. C. N. 2018a, *A&A*, 614, A14
 Reinoso, B., Schleicher, D. R. G., Fellhauer, M., Klessen, R. S., & Boekholt, T. C. N. 2018b, *AAP*, 614, A14
 Reinoso, B., Schleicher, D. R. G., Fellhauer, M., Leigh, N. W. C., & Klessen, R. S. 2020, *A&A*, 639, A92
 Renaud, F., Bournaud, F., & Duc, P.-A. 2015, *MNRAS*, 446, 2038
 Ricarte, A. & Natarajan, P. 2018, *MNRAS*, 481, 3278
 Rizzuto, F. P., Naab, T., Rantala, A., et al. 2023, *MNRAS*, 521, 2930
 Rizzuto, F. P., Naab, T., Spurzem, R., et al. 2021, *MNRAS*, 501, 5257
 Rodriguez, C. L., Weatherford, N. C., Coughlin, S. C., et al. 2022, *ApJS*, 258, 22
 Rodriguez, C. L., Zevin, M., Amaro-Seoane, P., et al. 2019, *PhRvD*, 100, 043027
 Ryu, T., Krolik, J., Piran, T., & Noble, S. C. 2020a, *ApJ*, 904, 99
 Ryu, T., Krolik, J., Piran, T., & Noble, S. C. 2020b, *ApJ*, 904, 100
 Ryu, T., Krolik, J., Piran, T., & Noble, S. C. 2020c, *ApJ*, 904, 101
 Sakurai, Y., Yoshida, N., Fujii, M. S., & Hirano, S. 2017, *MNRAS*, 472, 1677
 Sander, A. A. C., Vink, J. S., & Hamann, W. R. 2020, *MNRAS*, 491, 4406
 Sanders, R. H. 1970, *ApJ*, 162, 791
 Scoggins, M. T., Haiman, Z., & Wise, J. H. 2023, *MNRAS*, 519, 2155
 Shapiro, S. L. & Teukolsky, S. A. 1985, *ApJ*, 292, L41
 Solar, P. A., Reinoso, B., Schleicher, D. R. G., Klessen, R. S., & Banerjee, R. 2025, arXiv e-prints, arXiv:2505.19321
 Somerville, R. S., Yung, L. Y. A., Lancaster, L., et al. 2025, arXiv e-prints, arXiv:2505.05442
 Souvatzis, L., Rantala, A., & Naab, T. 2025, *MNRAS*, 539, 45
 Spitzer, Lyman, J. & Saslaw, W. C. 1966, *ApJ*, 143, 400
 Spitzer, Lyman, J. & Stone, M. E. 1967, *ApJ*, 147, 519
 Spurzem, R. 1999, *Journal of Computational and Applied Mathematics*, 109, 407
 Spurzem, R. & Kamlah, A. 2023, *Living Reviews in Computational Astrophysics*, 9, 3
 Stiefel, E. & Kustaanheimo, P. 1965, *Journal für die reine und angewandte Mathematik*, 218, 204
 Stodolkiewicz, J. S. 1982, *Acta Astron.*, 32, 63
 Stodolkiewicz, J. S. 1986, *Acta Astron.*, 36, 19
 Stone, N. C. & Metzger, B. D. 2016, *MNRAS*, 455, 859
 Stone, N. C., Vasiliev, E., Kesden, M., et al. 2020, *Space Sci. Rev.*, 216, 35
 Tacchella, S., Eisenstein, D. J., Hainline, K., et al. 2023, *ApJ*, 952, 74
 Tan, J. C. & McKee, C. F. 2004, *ApJ*, 603, 383
 Tsiatsiou, S., Sibony, Y., Nandal, D., et al. 2024, *A&A*, 687, A307
 Übler, H., Maiolino, R., Pérez-González, P. G., et al. 2024, *MNRAS*, 531, 355
 Vanzella, E., Castellano, M., Bergamini, P., et al. 2022a, *A&A*, 659, A2
 Vanzella, E., Castellano, M., Bergamini, P., et al. 2022b, *ApJ*, 940, L53
 Vanzella, E., Castellano, M., Bergamini, P., et al. 2022c, *ApJ*, 940, L53
 Vanzella, E., Claeysens, A., Welch, B., et al. 2023, *ApJ*, 945, 53
 Vergara, M. C., Askar, A., Kamlah, A. W. H., et al. 2025, arXiv e-prints, arXiv:2505.07491
 Vergara, M. C., Escala, A., Schleicher, D. R. G., & Reinoso, B. 2023, *MNRAS*, 522, 4224
 Vergara, M. C., Schleicher, D. R. G., Escala, A., et al. 2024, arXiv e-prints, arXiv:2405.12008
 Vergara, M. Z. C., Schleicher, D. R. G., Boekholt, T. C. N., et al. 2021, *A&A*, 649, A160
 Vink, J. S. 2018, *A&A*, 615, A119
 Vink, J. S. & de Koter, A. 2002, *A&A*, 393, 543
 Vink, J. S. & de Koter, A. 2005, *AAP*, 442, 587
 Vink, J. S., de Koter, A., & Lamers, H. J. G. L. M. 2001, *A&A*, 369, 574
 Volonteri, M., Haardt, F., & Madau, P. 2003, *ApJ*, 582, 559
 Wang, L., Fujii, M. S., & Tanikawa, A. 2021, *MNRAS*, 504, 5778
 Wang, L., Gieles, M., Baumgardt, H., et al. 2024, *MNRAS*, 527, 7495
 Wang, L., Kroupa, P., Takahashi, K., & Jerabkova, T. 2020a, *MNRAS*, 491, 440
 Wang, L., Kroupa, P., Takahashi, K., & Jerabkova, T. 2020b, *MNRAS*, 491, 440
 Wang, L., Spurzem, R., Aarseth, S., et al. 2016, *MNRAS*, 458, 1450
 Wang, L., Spurzem, R., Aarseth, S., et al. 2015, *MNRAS*, 450, 4070
 Wang, L., Tanikawa, A., & Fujii, M. S. 2022, *MNRAS*, 509, 4713

Appendix A: Treatment of the rejuvenation of a star through collisions

The rejuvenation of a main-sequence star upon collisions with other main-sequence stars was numerically implemented by Hurley et al. (2002, 2005). The main motivation for the introduction was to provide a proper treatment of blue straggler stars. These stars consistently find themselves above a stellar populations MS turn-off point (see e.g., for observational evidence, check Giesers et al. 2018). This implies that the effective age, A_{MS} , of these MS stars after a collision and a merger, is younger than the average age of the stellar population. In our models, which provide many collisions of a VMS with small mass MS stars, this treatment is not correct for the VMS, as the mass ratio q ,

$$q = \frac{M_{\text{MS},2}}{M_{\text{MS},1}} \quad (\text{A.1})$$

becomes very small (i.e., $q \ll 1$).

If we work under the base assumption that hydrogen in the MS core is uniformly distributed, then, after a collision, we have a convective mixing of the hydrogen fuel from envelope to core. The BSE code terminates the MS phase of the star and enters the Hertzsprung gap (HG) phase after 10 % of the total amount of hydrogen in the MS star has been burned (Hurley et al. 2000, 2005), the computational application is described below. We first consider the collision of two MS stars with (effective) ages $A_{\text{MS},1}$ and $A_{\text{MS},2}$, MS life-times $\tau_{\text{MS},1}$ and $\tau_{\text{MS},2}$, as well as masses $M_{\text{MS},1}$ and $M_{\text{MS},2}$, respectively. Here, the subscripts 1 and 2 denote the primary (and more massive) MS star and the secondary star, respectively. The collision produces the "third" MS star with effective age $A_{\text{MS},3}$, MS life time $\tau_{\text{MS},3}$ and mass $M_{\text{MS},3}$. If we know these parameters, (as suggested in Hurley et al. 2005) we can evaluate the final effective age $A_{\text{H,MS},3}$ of the produced MS star with their equation (see also Glebbeek et al. 2008, for more information). This treatment works well for MS collisions that have mass ratios $q \approx 1$, which might be expected for many blue stragglers.

Here we have updated the traditional treatment, finding the age of the newly formed MS star as:

$$F_q = 1.0 - q \cdot (1.0 - 0.1/(1 + q)), \quad (\text{A.2})$$

$$A_{\text{MS},3} = \tau_{\text{MS},3} \cdot F_q \cdot (A_{\text{MS},1}/\tau_{\text{MS},1} - q \cdot A_{\text{MS},2}/\tau_{\text{MS},2}). \quad (\text{A.3})$$

This treatment for the age of the VMS ensures that (i) if $q \rightarrow 1$ and $F_q \rightarrow 1$ (that is, the two colliding stars have similar masses), we get Eq. A.3, while (ii) for $q \rightarrow 0$ and $F_q \rightarrow 0$ (that is, the primary star is much more massive than the secondary star) the age of the VMS does not change significantly. This approach improves on the traditional treatment by ensuring a physically reasonable behavior in the limit $q \ll 1$. In such cases, the secondary star contributes very little mass, and thus the merger product should retain an age close to that of the more massive primary. The introduction of the factor F_q ensures that the rejuvenation is suppressed when q is small, preventing an unrealistically young apparent age for the merger product. In contrast, earlier models lacking such a correction could significantly underestimate the age in this regime, resulting in overly rejuvenated stars even when the secondary's contribution is negligible.

Appendix B: Treatment of collisions in MOCCA

In the models with the shortest crossing and relaxation times considered in this work, specifically the R0005N50K, R001N100K, and R001N250K runs (see Fig. B.1), we found that the standard MOCCA collision treatment, based on local density and cross-section estimates, leads to unrealistically rapid growth of the VMS. In particular, before our improvements, the mass of the VMS would increase by more than a factor of two to three, compared to results from direct N -body simulations, indicating that collisions with VMS were overpredicted in these extreme regimes. To address this, we developed and implemented an improved, physically motivated treatment for VMS collisions in these high-density, low- N models. After introducing this new prescription, the MOCCA results for VMS growth were brought into good agreement with direct N -body simulations.

In standard MOCCA simulations, the probability for a collision between two single stars is computed using the cross-section formalism:

$$P_{\text{coll}} = 0.5 C p_{\text{max}}^2 n u \Delta t \quad (\text{B.1})$$

where C is a normalization constant, p_{max} is the maximum impact parameter (related to the sum of stellar radii and gravitational focusing), n is the local number density, u is the relative velocity, and Δt is the timestep. The collision outcome is then determined probabilistically, and, if a collision occurs, the two stars are merged.

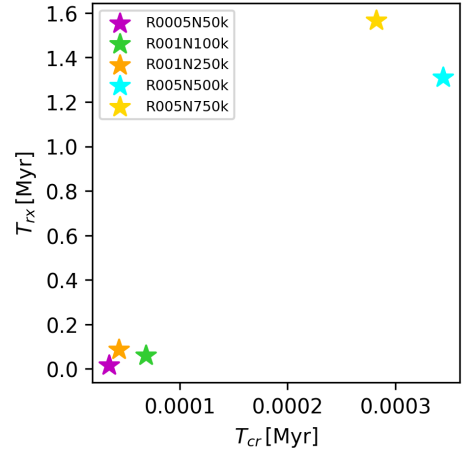


Fig. B.1. Initial half-mass relaxation time (T_{rx}) versus initial crossing time (T_{cr}) for the five cluster models simulated in this work. The three models with the shortest relaxation and crossing times (R0005N50k, R001N100k, and R001N250k) required a modified collision treatment, since the standard local-density-based prescription significantly overestimates the collision rate in these extreme regimes

For these compact models ($R_h \leq 0.01$ pc) with relatively low number of stars, this cross-section-based approach becomes inaccurate because the presence of a VMS can dominate the local gravitational potential, invalidating the assumptions of the local density formalism and leading to overestimated collision rates. To address this limitation, we introduced a more physically motivated, two-body treatment for collisions involving VMSs, defined here as stars with $M \geq M_{\text{VMS,th}}$, where $M_{\text{VMS,th}} = 500 M_{\odot}$ in our production runs. This new approach assumes that, in the presence of a dominant central VMS, gravitational focusing and two-body orbital dynamics, rather than the local stellar density, govern whether a close passage results in a physical collision. In this approach, instead of applying the probabilistic cross-section

formula, we explicitly compute the Keplerian orbital parameters for stars that are closest to each VMS in the system.

For each collision candidate pair where the primary star satisfies $M_1 \geq M_{\text{VMS,th}}$, we compute the specific energy and specific angular momentum of the secondary star (hereafter, “star 2”) with respect to the VMS (“star 1”):

$$\epsilon_2 = \frac{1}{2} (v_{r,2}^2 + v_{t,2}^2) - \frac{GM_1}{r_2} \quad (\text{B.2})$$

$$\ell_2 = r_2 |v_{t,2}| \quad (\text{B.3})$$

where $v_{r,2}$ and $v_{t,2}$ are the radial and tangential velocities of star 2 with respect to the VMS, r_2 is its distance from the VMS, and G is the gravitational constant (set to unity in code units).

The pericenter distance of star 2 with respect to the VMS is then given by

$$r_{p,2} = \frac{-GM_1 + \sqrt{(GM_1)^2 + 2\epsilon_2\ell_2^2}}{2\epsilon_2}. \quad (\text{B.4})$$

If $\epsilon_2 \approx 0$ (parabolic approach), we instead use

$$r_{p,2} = \frac{\ell_2^2}{2GM_1}. \quad (\text{B.5})$$

A physical collision is deemed to occur if $r_{p,2} \leq R_1 + R_2$, where R_1 and R_2 are the radii of the two stars. In this case, the collision is forced ($P_{\text{coll}} = 1$), bypassing the original probabilistic cross-section calculation. If the pericenter is greater than the sum of the radii, no collision occurs.

The modified treatment is applied only when the more massive star in the pair exceeds the VMS mass threshold. For other star pairs, we use the original cross-section-based approach. For efficiency, and to mimic the high rate of encounters expected in extreme environments, this pericenter criterion is applied to a fixed number of the nearest neighbours of the VMS during each timestep. Specifically, we use the 30 nearest stars for the R0005N50k and R001N100k models, and 100 neighbours for the R001N250k run. All other aspects of the collision and merger handling, such as mass loss, rejuvenation, and product type, remain as in the standard MOCCA prescription.

We also applied this modified routine to the R005N500k model, where the pericenter test was used for the 200 nearest neighbours of each VMS. In that case, the combination of a larger neighbour set and a smaller timestep led to significantly improved agreement between MOCCA and direct N -body results for VMS growth. Without the new treatment, for the R005N500k run, the standard collision prescription overestimated the IMBH mass at formation by about $5,000 M_\odot$ ($25,000 M_\odot$ versus $20,000 M_\odot$ in the direct N -body simulation).

For the R0075N750k model, however, we found that the new prescription underpredicted the final IMBH mass relative to the direct N -body result. Therefore, for this highest- N case, we retained the original MOCCA collision treatment. As shown previously by Vergara et al. (2025), the agreement between MOCCA and direct N -body simulations is reasonable for large- N models when the standard probability-based collision treatment is used. In such high- N clusters, the larger number of massive stars provides a significant reservoir of potential collision partners for the VMS, enabling continuous growth over several Myr. Additionally, the longer relaxation time in these systems means that mass segregation and the subsequent delivery of massive stars to the cluster center proceeds more gradually, supporting a more extended phase of VMS growth.

In summary, we replaced the cross-section-based probabilistic collision criterion with a two-body pericenter test for VMSs, as described by the equations above. This suppresses artificially high collision rates in extreme-density, low- N runs and yields a more physical growth rate for VMSs, bringing the MOCCA results into agreement with the direct N -body simulations. We emphasize that this represents only a first step toward developing an improved and more general treatment for collisions involving a VMS or a central IMBH. In future work, we plan to implement and test more sophisticated prescriptions, guided by systematic comparisons with direct N -body simulations.

Appendix C: Number of collisions and mass contribution

We analyze the number of stellar collisions and their mass contributions to VMS and BH seed formation, from both simulation codes.

Fig. C.1 presents histograms of the number of collisions across different mass ranges. The results from the N -body simulations are shown with solid bars, while those from the MOCCA code are indicated with hatched bars. The histogram bins correspond to the following mass intervals: < 0.1 , $0.1-1$, $1-10$, $10-100$, and $> 100 M_\odot$. Each panel represents a different model from top to bottom: R0005N50k, R001N100k, R001N250k, R005N500k and R005N750k. The number of collisions for the different mass range in each models is listed below, the first set corresponds to the N -body, and the second to the MOCCA results:

- Model R0005N50k:
 N -body: 92, 762, 200, 76, 5
 MOCCA: 54, 351, 193, 108, 7
- Model R001N100k:
 N -body: 139, 1046, 223, 156, 7
 MOCCA: 12, 145, 96, 143, 8
- Model R001N250k:
 N -body: 571, 4156, 796, 404, 29
 MOCCA: 71, 508, 268, 280, 55
- Model R005N500k:
 N -body: 491, 3503, 677, 383, 46
 MOCCA: 342, 2357, 494, 358, 45
- Model R005N750k:
 N -body: 1072, 7649, 1442, 685, 71
 MOCCA: 271, 2176, 1124, 767, 79

Fig. C.2 presents histograms of the mass contribution to the VMS and BH seed formation. The bar styles, panels, bin mass intervals, and bullet points are the same as in Fig. C.1, the results are:

- Model R0005N50k:
 N -body: 8.20, 265.42, 722.30, 2237.57, 709.96 M_\odot
 MOCCA: 4.74, 125.72, 715.84, 2921.03, 842.85 M_\odot
- Model R001N100k:
 N -body: 12.41, 336.44, 682.50, 5082.01, 920.88 M_\odot
 MOCCA: 1.09, 53.68, 396.52, 5344.29, 1055.53 M_\odot
- Model R001N250k:
 N -body: 50.99, 1377.53, 2355.33, 12 805.41, 4039.95 M_\odot
 MOCCA: 6.32, 180.35, 1042.07, 10 343.75, 8502.78 M_\odot
- Model R005N500k:
 N -body: 43.77, 1146.33, 2067.01, 14 622.21, 5835.47 M_\odot
 MOCCA: 30.56, 789.12, 1671.15, 13 943.06, 5420.96 M_\odot

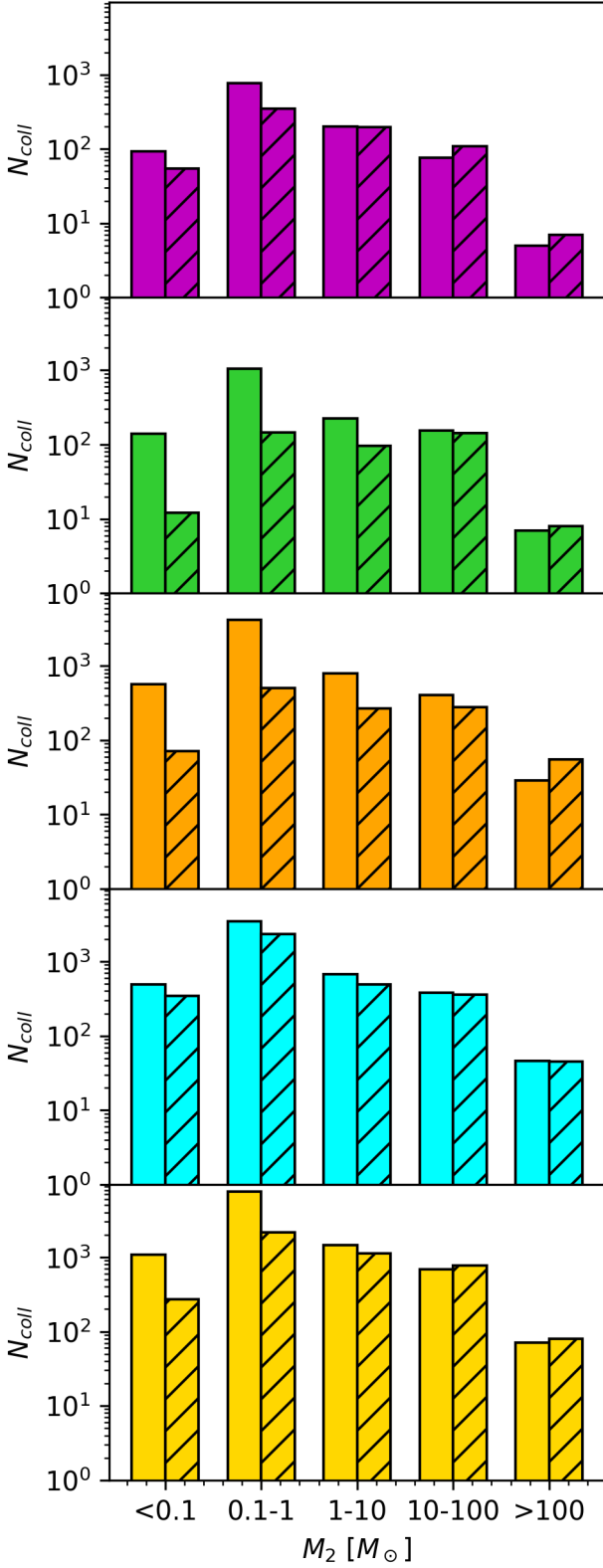


Fig. C.1. Histograms showing the number of collisions contributing to VMS/BH seed formation. The mass bins are: $< 0.1 M_{\odot}$, $0.1-1 M_{\odot}$, $1-10 M_{\odot}$, $10-100 M_{\odot}$, and $> 100 M_{\odot}$. Results are shown for both the N-body simulations (solid bars) and the MOCCA simulations (hatched bars). From top to bottom, the models are R0005N50k, R001N100k, R001N250k, R005N500k, and R005N750k.

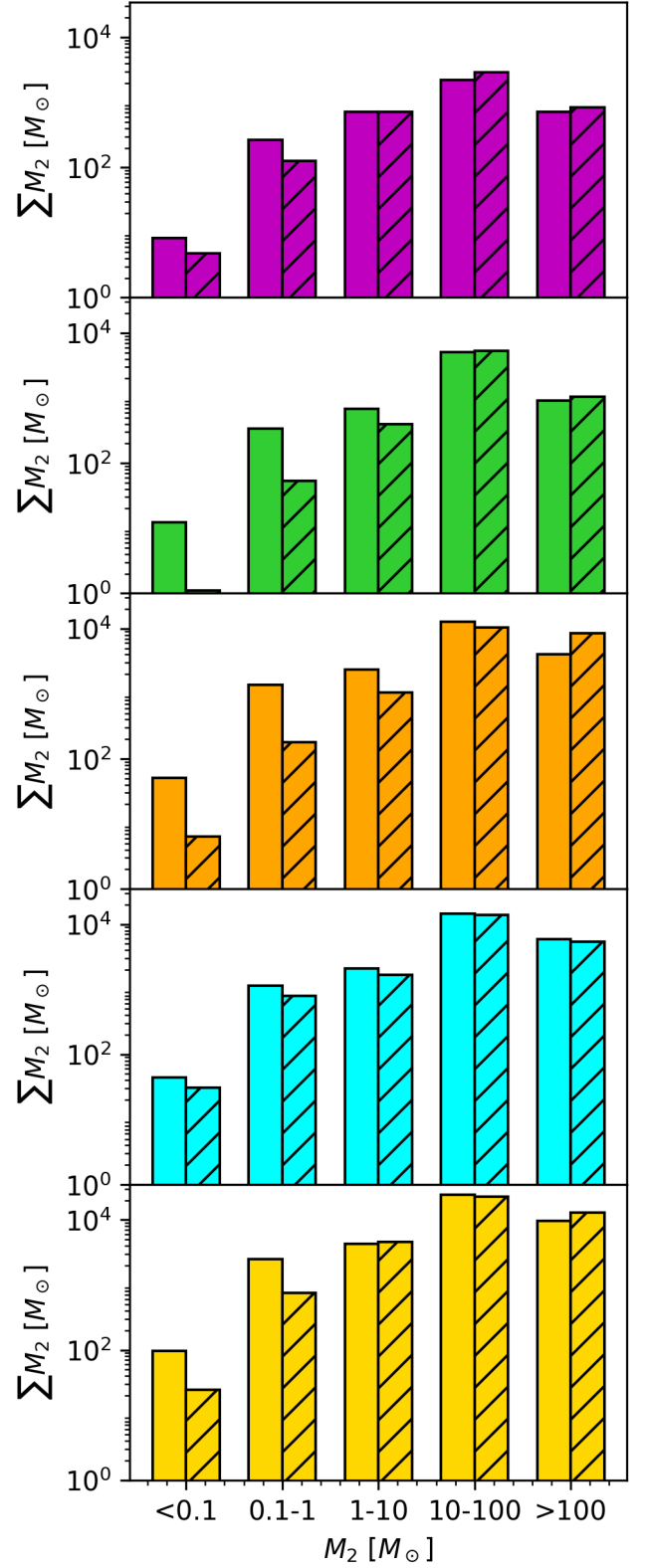


Fig. C.2. Histograms showing the cumulative mass contributed to VMS/BH seed formation. The mass bins and bar styles are the same as in Fig. C.1.

– Model R005N750k:

N-body: 95.80, 2490.73, 4241.25, 24 527.13, 9636.05 M_{\odot}
MOCCA: 24.21, 754.99, 4565.79, 22 993.53, 12 946.69 M_{\odot}

Both codes produce different numbers of collisions within the mass interval bins, resulting in varying mass contributions, despite starting from the same initial conditions. The models R0005N50k, R001N100k, R001N250k, R005N500k, and R005N750k initially contain 5, 5, 30, 57, and 79 stars with masses $> 100 M_{\odot}$, respectively. However, in the MOCCA simulations, the VMS shows a greater contribution from stars with masses $> 100 M_{\odot}$ in the R0005N50k, R001N100k, and R001N250k models. This occurs because the standard MOCCA prescription forms massive stars earlier, which then sink and collide with the VMS. The high densities presented in these clusters, quickly form a VMS in the center that bound several low-mass stars. The new collision treatment implemented in MOCCA, implies that if a star presents a pericenter distance slightly greater than the sum of the radii of its two stars, it is not considered as a candidate to collide with the VMS, however, due to the standard collision treatment, they will be candidates to collide with other stars that present similar conditions (i.e. $r_{p,2} > R_1 + R_2$), thus implying that they might collide with each other, forming a more massive star, that later sink to the center. This extremely dense regime for the star cluster challenges the standard collision treatment in MOCCA, this new update is the first attempt to treat collisions in the proximity of a single massive object at the center, however, the general agreement on the final outcome of both codes is a very good sign that we are on the right track, in the future we will further improve the treatment in MOCCA to obtain better overall agreement for the number of collisions we see with direct N -body.

Appendix D: Number of escapers and type of direct collisions in N -body

We analyze the number of escapers, binary and hyperbolic collisions across our models. This analysis is limited to N -body simulations. In MOCCA, all recorded collisions are treated as hyperbolic encounters, since the code does not explicitly follow the orbital motion of stars, thus is not possible to distinguish between binary and hyperbolic collisions.

In Fig. D.1, models R0005N50k, R001N100k, and R001N250k present hyperbolic collisions within the first 100 yr, while binary collisions appear later around 1000 yr. Notably, the appearance of escaping stars coincides with the onset of binary collisions. Model R005N500k, both hyperbolic and binary collisions occur almost simultaneously at early times. However, hyperbolic encounters dominate for the first few thousand years. Still, the number of escapers begins to rise significantly once the rate of binary collisions increases. Model R005N750k, also shows early hyperbolic collisions, with a single escape occurring prior to any binary collisions. Nevertheless, a notable increase in escapers follows the onset of binary encounters.

In general, we observe that hyperbolic collisions generally occur earlier than binary collisions. The number of escaping stars begins to increase notably as the number of binary collisions rises. This suggests that the stellar escapes are primarily driven by binary interactions.

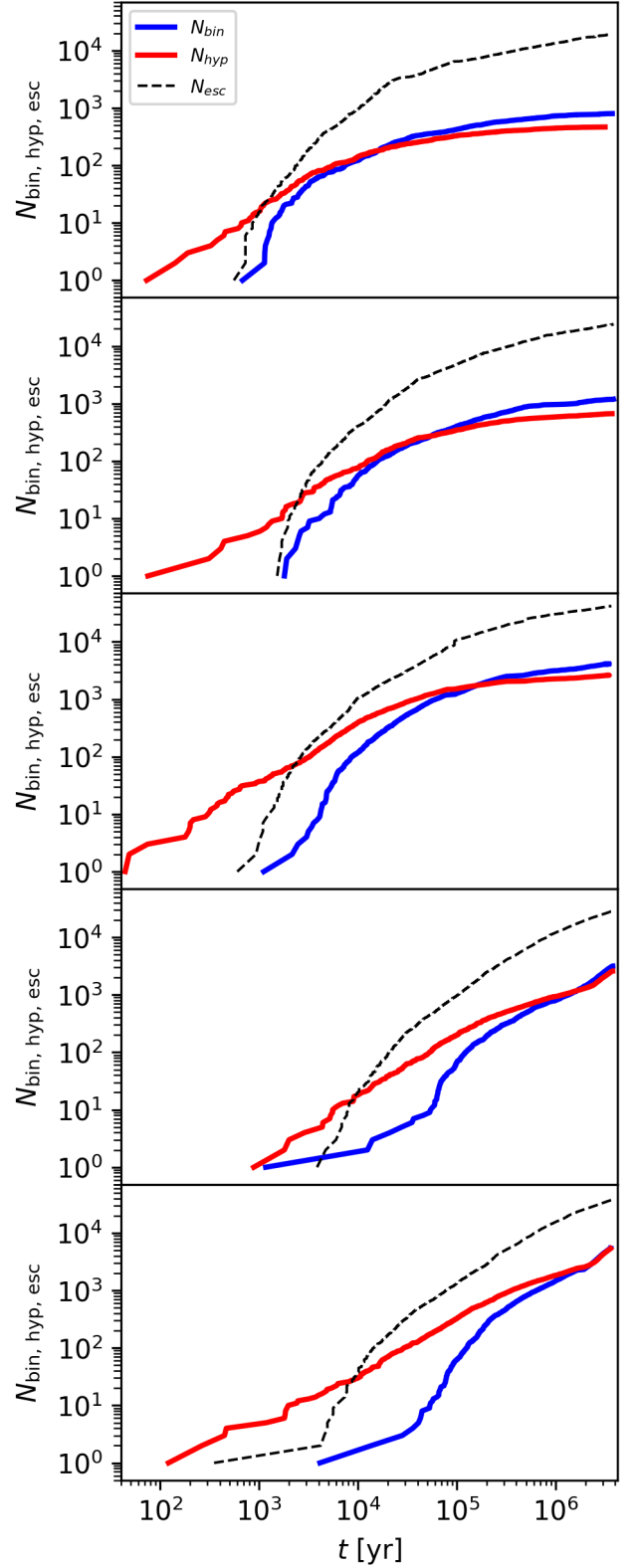


Fig. D.1. Time evolution of the number of escaping stars (dashed black line) and the number of binary (solid blue line) and hyperbolic (solid red line) collisions. From top to bottom, the models are R0005N50k, R001N100k, R001N250k, R005N500k, and R005N750k.